IOP PUBLISHING INVERSE PROBLEMS

Inverse Problems **29** (2013) 054005 (35pp) doi:10.1088/0266-5611/29/5/054005

Reduction of ionospheric distortions for spaceborne synthetic aperture radar with the help of image registration

Mikhail Gilman[1], **Erick Smith**[1] **and Semyon Tsynkov**[1,2]

[1] Department of Mathematics, North Carolina State University, Campus Box 8205, Raleigh, NC 27695, USA
[2] Moscow Institute of Physics and Technology, Dolgoprudny, Moscow 141700, Russia

E-mail: tsynkov@math.ncsu.edu

Received 7 August 2012, in final form 29 December 2012
Published 18 April 2013
Online at stacks.iop.org/IP/29/054005

Abstract

We propose a robust technique for reducing the ionospheric distortions in spaceborne synthetic aperture radar (SAR) images. It is based on probing the terrain on two distinct carrier frequencies. Compared to our previous work on the subject (Smith and Tsynkov 2011 *SIAM J. Imaging Sciences* **4** 501–42), the increase in robustness is achieved by applying an area-based image registration algorithm to the two images obtained on two frequencies. This enables an accurate evaluation of the shift between the two images, which, in turn, translates into an accurate estimate of the total electron content and its along-track gradient in the ionosphere. These estimates allow one to correct the matched filter and thus improve the quality of the image. Moreover, for the analysis of SAR resolution in the current paper we take into account the Ohm conductivity in the ionosphere (in addition to its temporal dispersion), and also consider the true Kolmogorov spectrum of the ionospheric turbulence, as opposed to its approximate representation that we have used previously.

1. Introduction

Synthetic aperture radar (SAR) uses microwave electromagnetic pulses for imaging the surface of the Earth from airplanes or satellites. To actually build the image, i.e. to reconstruct the ground reflectivity function, the raw signals scattered from the Earth's surface and received by the radar antenna need to be processed by means of a matched filter [1]. The filter is called matched because its parameters are supposed to match those of the received signal in a certain way. Mathematically, one can show that the received signal can approximately be interpreted as a Fourier transform of the ground reflectivity function, whereas filtering that yields the image is analogous to the inverse transform.

When the signal of a spaceborne radar travels between the satellite and the ground, it becomes subject to temporal dispersion in the Earth's ionosphere [2]. The dispersion distorts the signal, and if the filter does not account for that, a mismatch occurs and the quality of the

image deteriorates [3]. The extent of deterioration becomes smaller as the ratio of the Langmuir frequency of the ionospheric plasma to the carrier frequency of the radar decreases. Therefore, many modern spaceborne SAR instruments (e.g., TerraSAR-X) operate in the X-band, i.e. at frequencies of around 10 GHz.

However, radar operating at lower carrier frequencies, in particular, in the UHF or even VHF band, i.e. in the range of hundreds of megahertz (also referred to as the P-band [4]), has at least one key advantage, which is a better surface/foliage penetrating capability. At the same time, the images are much more sensitive to ionospheric distortions. Hence, an effort aimed at developing the means for reducing or removing those distortions is justified. Some performance criteria for the correction of ionospheric effects in SAR images obtained at low frequencies are discussed in [5].

In [3, 6], we have analyzed the propagation of radar pulses (linear upchirps) in the ionosphere modeled as weakly dispersive dilute cold plasma. The transverse electric field in such a medium is governed by the Klein–Gordon equation (dispersive wave equation), see formula (1). Our analysis has enabled an accurate quantification of the group delay and phase advance that characterize the propagation, as well as of the changes in the chirp duration and rate, for both homogeneous and inhomogeneous ionosphere. As such, it has led to a precise description of the mismatches between the received signal and the matched filter. Those mismatches have been shown to be the primary source of image distortions, and the distortions have been quantified in terms of how the image resolution and sharpness depend on the parameters of the ionospheric plasma, primarily its total electron content (TEC) along the signal trajectory. This part of the study involved building and analyzing the generalized ambiguity function (GAF) for the radar that would take into account the dispersive propagation in the ionosphere.

We have also shown in [6] that when probing the terrain, and hence the ionosphere, on two distinct carrier frequencies, the resulting two images, while both incorrect *per se*, can be used to reconstruct the unknown TEC. Specifically, a given object or feature in the scene will be displaced from its true position if imaged through the ionosphere. Considering the same object or feature imaged on two carrier frequencies, we can write down a system of equations in which the two observed distances to the object will be the data and the true distance and the TEC will be the unknowns. Solving for the TEC, we can obtain it as a function of the shift between the two images.

Having derived the TEC at the precise time and place the image was taken (this is very important, because the parameters of the ionosphere may change rapidly), we can correct the matched filter by introducing the actual phase and group travel times, as well as the new chirp rate, computed via the TEC. Then, by re-processing the raw data with the new filter, we can obtain an improved image. By evaluating and analyzing the new GAF that is built with the help of the corrected filter, we have been able to show that the quality of the image indeed becomes better. Specifically, the distortions in range are completely removed, whereas the distortions in azimuth are removed in their deterministic part, i.e. in the part that is not due to the turbulent fluctuations of the electron number density in the ionosphere. The reason for this 'unevenness' between the range and azimuth is that the performance of a spaceborne SAR in range is practically not affected by the ionospheric turbulence due to the ergodicity of the random field that represents the fluctuations, whereas the performance in azimuth is sensitive to both the deterministic and random components of the electron number density.

It is to be noted that the idea of dual carrier probing for quantifying the ionospheric distortions of satellite radio signals has been used in the GPS community for quite some time. For example, the near-realtime GPS-derived global TEC maps are available on-line at http://swaciweb.dlr.de. In the literature, the study [7] discusses general effects of the ionosphere

on the satellite to land radio propagation in the UHF and L bands. Paper [8] exploits the TEC data obtained from GPS-based measurements for evaluating the extent of defocusing in space-based SAR images. The fundamental difference between the GPS and SAR though is that in GPS there is a 'sufficiently smart' receiver on the ground that can interpret the data it receives on two frequencies. In SAR, on the other hand, the imaged terrain is assumed completely passive. Moreover, no artificial targets with *a priori* known characteristics are, generally speaking, available, and the parameters of the ionosphere must be determined from the same data that are used to form the image itself (scattered field received by the antenna in orbit).

Unlike in GPS, the application of dual carrier probing for quantifying and mitigating the distortions of spaceborne SAR images is new, see [3, 6]. The key consideration is precisely the use of the same (redundant) data for both the image formation and the TEC reconstruction. Indeed, if the TEC data are acquired at a different location and/or different time, they may reflect a different state of the ionosphere and hence appear not particularly helpful for correcting the matched filter to be used for a given image.

Prior to our work [3, 6], we were aware of only one paper [9] that briefly touches upon the idea of two frequencies for SAR, and also of an equally brief comment in [10, page 381]. The authors of [9] suggest that the two frequencies can be taken from the available bandwidth, but never actually develop the approach beyond mentioning it as a potential strategy for obtaining the TEC. Another group of publications [11–14] discusses and demonstrates the use of two sub-bands in the context of SAR interferometry. Some of the methods of [11–14] also utilize the aforementioned difference in the displacement between the two images. The interferometric approach, however, allows one to reconstruct only the differential TEC[3], although with very high accuracy [13, 14]. Given the satellite revisit time of several days that characterizes both existing and future SAR systems, and the volatility of the ionosphere, the requirement of having a repeat acquisition makes the acquired information less valuable for many practical applications.

Several alternative approaches to deriving the ionospheric TEC have also been proposed in the literature. Some of them are motivated by the launch of the Japanese Advanced Land Observation Satellite (ALOS) that carries a phased array SAR instrument (PALSAR) operating in the L-band. In [15] and [16], it is proposed to use the Faraday rotation for retrieving the TEC information from the fully polarimetric quad-channel SAR data, in the case that the corresponding SAR sensor provides this capability (which ALOS PALSAR does, see [17, section 10.4]). The authors of [15] also present the estimates of the group delays and phase advances for a non-turbulent ionosphere similar to those obtained in our earlier paper [3]. An even earlier publication discussing the effect of Faraday rotation on polarimetric SAR is [18]. Of course, if the fully polarimetric data are not available (or, otherwise, if polarimetry puts too high of a demand on storage, downlink capacity, etc), then the approach based on the Faraday rotation is not going to work. For example, the authors of [9] also rely on the Faraday rotation for TEC reconstruction, but emphasize that for other types of sensors (e.g., single channel), an explicit *a priori* estimate of the Faraday rotation is needed for introducing corrections. The authors of [11] indicate that in the absence of external information, one can use autofocus algorithms (see [19, section 3.9.1] or [20, 21]) to obtain the TEC, whereas the SAR system itself (L-band) can be efficient in obtaining the difference of the TEC distributions between the two radar acquisitions. The authors of [22] present two approaches; the first one involves a spaceborne radar operating at a very low frequency, below the Langmuir value, and is similar to the traditional ground-based sounding. The second one uses a higher frequency and derives the TEC information by analyzing the returns from the specially chosen bright point targets.

[3] It is the difference between the TEC distributions for two successive data acquisitions.

The authors of [23] employ a simplified model known as the ionospheric phase screen to analyze the effect of auroral arcs (special electron density irregularities) on spaceborne SAR images taken in the polar regions of the Earth. Finally, the authors of [24] introduce two methods for measuring the ionospheric TEC based on single-polarized data. The first one estimates the TEC from the phase error of the filter mismatch and requires high contrast strong point targets such as corner reflectors within an otherwise dark area; the second one requires two different interrogating waveforms, up and down linear chirps, and estimates the TEC from the path-delay differences between them. We note that none of these papers, see [15, 18, 11–14, 22–24], provides a comprehensive analysis of how the reconstructed TEC can be used for correcting the filter and subsequently improving the image.

As far as our own work is concerned, having demonstrated in [6] that the filter corrected by dual carrier probing indeed helps improve the image, we have proceeded to analyze the robustness and accuracy of the TEC reconstruction itself. The goal was to see what happens if the TEC is reconstructed not precisely, but with some error. The reason the TEC reconstruction may be prone to an error is that the formula for the TEC derived in [3, 6] by taking the two distances to a given object as the data appear poorly conditioned with respect to each individual distance. The first obvious remedy is to use several distinct objects instead of just one. In this case, the overall error can be reduced by a factor of $\sqrt{L}$, where L is the number of objects, see [6] (under a natural assumption that the values of the TEC computed for individual objects can be interpreted as independent random variables). However, a more promising approach is to use the technique known as area-based image registration [25]. It allows one to superimpose the two shifted images and obtain the shift as an independent quantity that is not related to the distance from the satellite. The accuracy of the modern registration techniques can be as high as a few per cent of the resolution pixel, see, e.g., [26–30].

In the current paper, we are showing that if an area-based image registration approach that uses the phase correlation (see, e.g., [31, 32]) is employed for evaluating the shift, then the robustness, and hence the accuracy of the TEC reconstruction, considerably improves. We obtain specific quantitative estimates of how the error in the value of the shift affects the error in the TEC and how the latter, in turn, affects the final quality of the image. Of course, these results withstand a natural 'backward compatibility check.' If we assume that there is no error in the value of the shift, then there will be no error in the value of the TEC, and eventually all the deterministic distortions of the image will be completely removed, as in [6].

For the rest of the paper, we will assume that the SAR imaging is done in the stripmap mode, and that it is broadside, i.e. that the antenna always points in the direction normal to the orbit, see figure 1. We will also employ the start–stop approximation for our analysis [1, 33]. In table 1, we present the key parameters and their typical values that we use hereafter. Note that along with the physical units of the TEC, cm^{-2}, used in table 1, engineering units defined as $1\,\mathrm{TECU} = 10^{12}\ \mathrm{cm}^{-2}$ can often be found in the literature. In section 2, we analyze the mechanism of distortions for the case of vertically stratified and horizontally homogeneous ionosphere. In section 3, we take into account a possible horizontal variation of the ionosphere. In section 4, we introduce the dual carrier probing as a way of reconstructing the characteristics of the ionosphere (the TEC and the first moment of the azimuthal gradient of the electron number density), and show how the robustness of reconstruction can be improved with the help of image registration. In section 5, we show how the filter can be corrected using the ionosphere parameters obtained by dual carrier probing, and how the corrected filter helps improve the quality of the image. In section 6, we analyze the effect of ionospheric turbulence, and in section 7, we draw some conclusions and discuss future work.

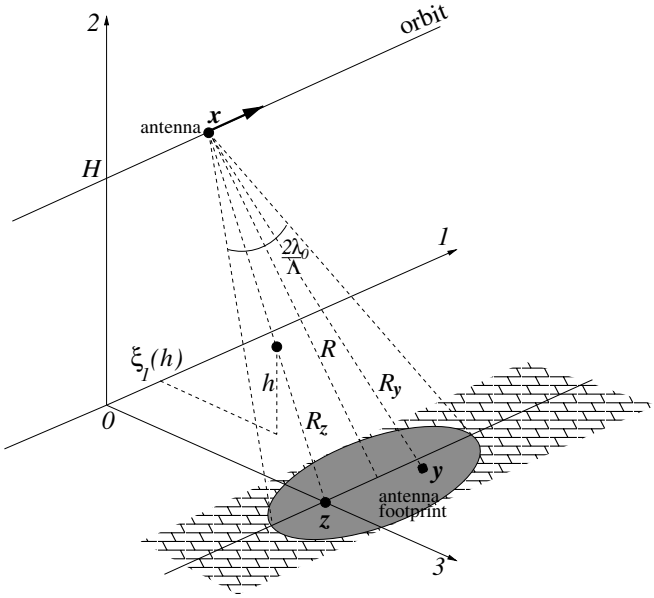

Figure 1. Schematic for the broadside stripmap SAR imaging.

Table 1. Typical values of parameters throughout this paper.

Parameter	Notation	Typical value	Reference
Radar carrier frequency	$\frac{\omega_0}{2\pi}$	300 MHz	(2)
Carrier wavelength	$\lambda_0 = \frac{2\pi c}{\omega_0}$	1 m	(2)
Bandwidth	$\frac{B}{2\pi}$	8 MHz	(6)
Pulse (chirp) duration	τ	5×10^{-5}s	(6)
Pulse repetition frequency	f_{p}	2 kHz	page 7
Total electron content in the ionosphere	N_H	5×10^{13} cm^{-2}	(25)
Plasma electron (Langmuir) frequency	$\frac{\omega_{\mathrm{pe}}}{2\pi}$	9 MHz	(1)
Collision frequency in the ionosphere	γ	10^5 Hz	(26), (B.1)
Satellite velocity	v_{SAT}	7.6 km s^{-1}	page 7
Length of synthetic aperture	L_{SA}	50 km	page 7
One-way distance from orbit to target	R	1000 km	(43), figure 1
Orbit altitude	H	500 km	figure 1
Incidence angle	$\cos\theta = \frac{H}{R}$	60°	figure 1
Registration accuracy, in resolution units	ζ_R, ζ_A	0.05	(69), (75)
Carrier frequency separation factor	Z	10%	(71)
Relative magnitude of fluctuations	M	5×10^{-3}	(81)
Outer scale of ionospheric turbulence	r_0	1 –10 km	(85)
Integral squared mean electron density	$N_{2,H}$	5×10^{19} cm^{-5}	(96)

2. Ionospheric distortions of SAR images

2.1. Propagation of radar signals and construction of a SAR image

High-frequency transverse electromagnetic waves in cold plasma are governed by the Klein–Gordon equation [3, appendix A]:

$$\frac{\partial^2\varphi}{\partial t^2} - c^2\Delta\varphi + \omega_{\mathrm{pe}}^2\varphi = 0, \quad \text{where} \quad \omega_{\mathrm{pe}} = \sqrt{\frac{4\pi e^2 n_{\mathrm{e}}}{m_{\mathrm{e}}}}. \tag{1}$$

In formula (1), n_e, m_e and ω_{pe} are the electron concentration (i.e. number density), mass and plasma frequency, respectively, and φ is any transverse component of the wave's electric or magnetic field. For $n_e = 0$ (i.e. in vacuum), equation (1) reduces to the standard wave (d'Alembert) equation. A plane electromagnetic wave has the form:

$$\varphi \sim e^{i(\omega t - kr)}, \tag{2}$$

where $\omega = 2\pi f$ is the angular frequency and k is the wavenumber, $|k| = 2\pi/\lambda = 2\pi f/c$. Substituting (2) into (1), we obtain the dispersion relation for the Klein–Gordon equation:

$$\omega^2 = \omega_{pe}^2 + c^2 k^2, \tag{3}$$

which yields the following expression for the dielectric constant ε of a cold plasma:

$$\frac{k^2 c^2}{\omega^2} = \varepsilon = 1 - \frac{\omega_{pe}^2}{\omega^2}. \tag{4}$$

The phase and group velocities of high-frequency electromagnetic waves in a medium described by (3) differ from the speed of light:

$$\begin{aligned} v_{ph} &\stackrel{\text{def}}{=} \frac{\omega(k)}{k} = c\Big(1 + \frac{\omega_{pe}^2}{c^2 k^2}\Big)^{\frac{1}{2}} \approx c\Big(1 + \frac{\omega_{pe}^2}{2\omega^2}\Big), \\ v_{gr} &\stackrel{\text{def}}{=} \frac{d\omega(k)}{dk} = c\Big(1 + \frac{\omega_{pe}^2}{c^2 k^2}\Big)^{-\frac{1}{2}} \approx c\Big(1 - \frac{\omega_{pe}^2}{2\omega^2}\Big), \end{aligned} \tag{5}$$

where we have assumed that $\omega \gg \omega_{pe}$ (see table 1). From (5), we find that $v_{ph} > c$, which results in a 'phase advance,' and $v_{gr} < c$, which leads to a 'group delay.'

A single-frequency-modulated pulse emitted by SAR is often taken as a linear chirp:

$$\begin{aligned} &P(t) = A(t)\, e^{i\omega_0 t}, \quad \text{where} \quad A(t) = \chi_\tau(t)\, e^{i\alpha t^2} \\ &\qquad \text{and} \quad \chi_\tau(t) = \{1,\ t \in [-\tau/2, \tau/2], 0,\ \text{otherwise}. \end{aligned} \tag{6}$$

In formula (6), $\alpha = \frac{B}{2\tau}$ is the chirp rate, $\frac{B}{2\pi}$ is the bandwidth of the chirp and τ is its duration. The envelope $A(t)$ of the pulse is assumed to vary slowly compared to the fast carrier oscillation $e^{i\omega_0 t}$. For the chirp (6) that has originated at $\boldsymbol{x}$ and is propagating in vacuum ($\omega_{pe} = 0$ in (1)), the time evolution at z is given by the retarded potential of the d'Alembert operator:

$$\varphi(t, z) = \frac{1}{4\pi} \frac{P(t - |z - \boldsymbol{x}|/c)}{|z - \boldsymbol{x}|}. \tag{7}$$

Once the field (7) reaches the target, it gets scattered. As in [6], we assume that the scattering is linearized, so that each point z of the target is considered a source of the scattered field with intensity

$$\nu(z) \frac{\partial^2 \varphi(t, z)}{\partial t^2} \approx -\omega_0^2 \nu(z) \varphi(t, z), \tag{8}$$

where $\nu(z)$ is the target backscattering reflectivity. Thus, the scattered field received by the antenna at the same location $\boldsymbol{x}$ is given by

$$\psi(t, \boldsymbol{x}) \approx \iiint_{|\boldsymbol{x} - z| \leqslant ct} \tilde{\nu}(\boldsymbol{x}, z) A\,(t - 2|\boldsymbol{x} - z|/c)\ e^{i\omega_0 (t - 2|\boldsymbol{x} - z|/c)}\, dz, \tag{9}$$

where

$$\tilde{\nu}(\boldsymbol{x}, z) = -\frac{\omega_0^2}{16\pi^2} \frac{\nu(z)}{|\boldsymbol{x} - z|^2}. \tag{10}$$

The SAR image is obtained by first applying a matched filter to the received field (9). The matched filter is defined as follows. Assuming that there is a point scatterer at the reference

location $\boldsymbol{y}$, the resulting field at $(t, \boldsymbol{x})$ is obtained by substituting $\nu(z) = \delta(z - \boldsymbol{y})$ into formula (9):

$$\psi_1(t, \boldsymbol{x}) = -\frac{\omega_0^2}{16\pi^2} \frac{P(t - 2|\boldsymbol{x} - \boldsymbol{y}|/c)}{|\boldsymbol{x} - \boldsymbol{y}|^2}.$$

The filter is given by $\overline{P(t - 2|\boldsymbol{x} - \boldsymbol{y}|/c)}$, which is a complex conjugate of ψ_1 up to a constant factor $-\omega_0^2/16\pi^2$ and a slowly varying denominator. The idea of matching is to have the large phase cancel in the exponent (see (6)), as shown by our subsequent derivations. The application of this filter yields

$$\begin{aligned} I(\boldsymbol{y}) &= \int \overline{P(t - 2|\boldsymbol{x} - \boldsymbol{y}|/c)} \psi(t, \boldsymbol{x}) \, \mathrm{d}t \\ &= \iiint \underbrace{\int \overline{P(t - 2|\boldsymbol{x} - \boldsymbol{y}|/c)} P(t - 2|\boldsymbol{x} - z|/c) \, \mathrm{d}t}_{W(\boldsymbol{y}, z)} \; \tilde{\nu}(\boldsymbol{x}, z) \, \mathrm{d}z. \end{aligned} \tag{11}$$

The transformations (9) and (11) can be thought of as direct and inverse Fourier integral operators acting between $\psi(t, \boldsymbol{x})$ and $\tilde{\nu}(\boldsymbol{x}, z)$. The interior integral $W(\boldsymbol{y}, z)$ in the last expression of (11) is called the point spread function, see [1, 34]. The 'ideal' point spread function would be equal to $\delta(\boldsymbol{y} - z)$ so that the triple integral in (11) would result in $I(\boldsymbol{y}) \sim \tilde{\nu}(\boldsymbol{x}, \boldsymbol{y})$, and hence the inversion would be perfectly accurate. While this is not achievable in practice due to bandwidth and other limitations, the goal of the SAR signal processing is to make the point spread function as close to the idealized delta shape as possible in order to minimize the geometric distortions between the original unknown function $\nu(z)$ and the result of the inversion (i.e. the image) $I(\boldsymbol{y})$.

The next step in building the image is to sum up the contributions from a series of pulses emitted and received by the antenna at times/locations $(t_n, \boldsymbol{x}^n)$. If for each n, we process the signal and build the point spread function according to (11):

$$W_n(\boldsymbol{y}, z) = \int \overline{P(t - t_n - 2|\boldsymbol{x}^n - \boldsymbol{y}|/c)} P(t - t_n - 2|\boldsymbol{x}^n - z|/c) \; \mathrm{d}t, \tag{12}$$

then the overall GAF will be given by the coherent sum of the respective contributions (12):

$$W(\boldsymbol{y}, z) = \sum_{n=-N/2}^{N/2} W_n(\boldsymbol{y}, z). \tag{13}$$

The range of values of $\boldsymbol{x}^n, n = -N/2, \ldots, N/2$ (in the direction along the orbit), that contribute to the sum (13) is called the synthetic aperture of the radar L_{SA}. The actual number of terms N also depends on the pulse repetition frequency (see table 1) $N = f_{\mathrm{p}} L_{\mathrm{SA}}/v_{\mathrm{SAT}}$, and is usually of the order of several thousands. The synthetic aperture may not exceed the range of those $\boldsymbol{x}^n$ from which a given z on the ground is illuminated for a specific radiation pattern of the antenna, or equivalently, for which z happens to be inside the radar beam footprint on the ground, see figure 1. In the simplest case, the angular width of the antenna beam is $\sim \frac{2\lambda_0}{\Lambda}$, where Λ is the antenna size (about 10 m), see [3, appendix B], so that the size of the footprint is $\sim \frac{2\lambda_0}{\Lambda} R$ and $L_{\mathrm{SA}} \leqslant \frac{2\lambda_0}{\Lambda} R$.

One can show [1] that the GAF $W(\boldsymbol{y}, z)$ of (13) can approximately be represented as a product of the range factor:

$$W_R(\boldsymbol{y}, z) = \int \overline{A(t - 2|\boldsymbol{y} - \boldsymbol{x}^0|/c)} A(t - 2|z - \boldsymbol{x}^0|/c) \, \mathrm{d}t \tag{14}$$

and the azimuthal factor

$$W_A(\boldsymbol{y}, z) = \sum_{n=-N/2}^{N/2} \mathrm{e}^{2\mathrm{i}\omega_0(|\boldsymbol{y} - \boldsymbol{x}^n|/c - |z - \boldsymbol{x}^n|/c)} \tag{15}$$

so that

$$W(\boldsymbol{y}, z) \approx W_R(\boldsymbol{y}, z) \cdot W_A(\boldsymbol{y}, z).$$

If $\omega_{\mathrm{pe}} \neq 0$, then the propagation of waves governed by equation (1) is accompanied by temporal dispersion. The case of homogeneous dispersive ionosphere ($\omega_{\mathrm{pe}} = \mathrm{const}$) is analyzed in appendix A. Under the assumptions of a high carrier frequency, $\omega_0 \gg \omega_{\mathrm{pe}}$, and narrow bandwidth, $\omega_0 \gg B$, the pulse (6) propagating in the plasma with dispersion relation (3) is described by formula (A.14) (cf formula (7)):

$$\varphi(t, z) = \frac{1}{4\pi} \frac{P'(\boldsymbol{x}, z, \omega_0, t)}{|z - \boldsymbol{x}|}, \tag{16}$$

where

$$P'(\boldsymbol{x}, z, \omega_0, t) = A'(t - T_{\mathrm{gr}}(\boldsymbol{x}, z, \omega_0))\, \mathrm{e}^{\mathrm{i}\omega_0 (t - T_{\mathrm{ph}}(\boldsymbol{x}, z, \omega_0))} \quad \text{and} \quad A'(t) = \chi_{\tau'}(t)\, \mathrm{e}^{\mathrm{i}\alpha' t^2}. \tag{17}$$

The group and phase travel times T_{gr} and T_{ph} in (17) are defined as (see (A.14) and (5))

$$T_{\mathrm{gr}}(\boldsymbol{x}, z, \omega_0) = \frac{|\boldsymbol{x} - z|}{v_{\mathrm{gr}}(\omega_0)} \quad \text{and} \quad T_{\mathrm{ph}}(\boldsymbol{x}, z, \omega_0) = \frac{|\boldsymbol{x} - z|}{v_{\mathrm{ph}}(\omega_0)}, \tag{18}$$

and the new chirp duration τ' and rate α' are given by (see (A.12) and (A.13))

$$\tau' = \tau - \delta\tau = \tau - \frac{|\boldsymbol{x} - z|}{c} \frac{\omega_{\mathrm{pe}}^2}{\omega_0^2} \frac{B}{\omega_0} \quad \text{and} \quad \alpha' = \alpha + \delta\alpha = \frac{B}{2\tau} \left(1 + \frac{\delta\tau}{\tau}\right). \tag{19}$$

The case of inhomogeneous dispersive ionosphere, where the Langmuir frequency ω_{pe} depends on the altitude, was analyzed in [6, appendix B]. While the form of the propagating signal (16), (17) in this case does not change, the travel times become (cf formula (18))

$$T_{\mathrm{gr}}(\boldsymbol{x}, z, \omega_0) = \frac{|\boldsymbol{x} - z|}{\bar{v}_{\mathrm{gr}}(\omega_0)} \quad \text{and} \quad T_{\mathrm{ph}}(\boldsymbol{x}, z, \omega_0) = \frac{|\boldsymbol{x} - z|}{\bar{v}_{\mathrm{ph}}(\omega_0)}. \tag{20}$$

The modified phase and group velocities $\bar{v}_{\mathrm{ph}}$ and $\bar{v}_{\mathrm{gr}}$ in (20) are (cf formulae (5))

$$\bar{v}_{\mathrm{ph}}(\omega_0) = c \left(1 + \frac{1}{2} \frac{\bar{\omega}_{\mathrm{pe}}^2}{\omega_0^2}\right) \quad \text{and} \quad \bar{v}_{\mathrm{gr}}(\omega_0) = c \left(1 - \frac{1}{2} \frac{\bar{\omega}_{\mathrm{pe}}^2}{\omega_0^2}\right), \tag{21}$$

where $\bar{\omega}_{\mathrm{pe}}^2$ is the square of the Langmuir frequency averaged over the straightened signal path between the antenna and the target:

$$\bar{\omega}_{\mathrm{pe}}^2 = \frac{1}{|\boldsymbol{x} - z|} \int_z^{\boldsymbol{x}} \omega_{\mathrm{pe}}^2(s)\, \mathrm{d}s \equiv \frac{1}{R_z} \int_0^{R_z} \omega_{\mathrm{pe}}^2(s)\, \mathrm{d}s. \tag{22}$$

The quantity $\bar{\omega}_{\mathrm{pe}}^2$ of (22) also helps re-define the new chirp duration and the rate for the stratified ionosphere (cf formula (19)):

$$\tau' = \tau - \delta\tau = \tau - \frac{|\boldsymbol{x} - z|}{c} \frac{\bar{\omega}_{\mathrm{pe}}^2}{\omega_0^2} \frac{B}{\omega_0} \quad \text{and} \quad \alpha' = \alpha + \delta\alpha = \frac{B}{2\tau} \left(1 + \frac{\delta\tau}{\tau}\right). \tag{23}$$

Note that in integral (22), s is the distance along the straight line connecting z and $\boldsymbol{x}$. In the case where the electron number density depends only on the altitude h: $n_{\mathrm{e}} = n_{\mathrm{e}}(h)$, integral (22) reduces to (see figure 1)

$$\bar{\omega}_{\mathrm{pe}}^2 = \frac{1}{|\boldsymbol{x} - z|} \int_0^H \omega_{\mathrm{pe}}^2(h) \frac{\mathrm{d}h}{\cos\theta} = \frac{1}{H} \int_0^H \omega_{\mathrm{pe}}^2(h)\, \mathrm{d}h = \frac{4\pi e^2}{m_{\mathrm{e}}} \frac{N_H}{H}, \tag{24}$$

where H is the orbit altitude and

$$N_H \overset{\mathrm{def}}{=} \int_0^H n_{\mathrm{e}}(h)\, \mathrm{d}h \tag{25}$$

is the TEC in the ionosphere[4]. A more realistic case, where the ionosphere has a horizontal inhomogeneity as well, is analyzed in section 3, whereas the ionospheric turbulence is accounted for in section 6.

In addition to temporal dispersion, the propagation of radio waves in the ionosphere may be subject to Ohmic losses. In appendix B, we show that in the case of a lossy ionosphere, the propagating chirp (6) still has the form (16), but instead of (17) the numerator is given by (see formula (B.4))

$$P'(\boldsymbol{x}, z, \omega_0, t) = A'(t - T_{\rm gr}(\boldsymbol{x}, z, \omega_0))\, \mathrm{e}^{\mathrm{i}\omega_0 (t - T_{\rm ph}(\boldsymbol{x}, z, \omega_0))}\, \mathrm{e}^{-\frac{1}{2}\frac{|\boldsymbol{x}-z|}{c}\frac{\gamma\omega_{\rm pe}^2}{\omega_0^2}}, \tag{26}$$

where γ is the effective frequency of the particle collisions in the ionosphere [2]. For the typical parameters presented in table 1, including $|\boldsymbol{x} - z| \sim R$, the last exponential factor in (26) evaluates to $\mathrm{e}^{-0.15} \approx 0.86$, which means that the one-way signal attenuation due to the Ohmic losses in the ionosphere is about 14%. While not negligible by itself, this attenuation affects only the amplitude of the propagating chirp and does not affect its phase. Therefore, we will not be taking the Ohmic losses into account hereafter (as we effectively do not take into account the geometric attenuation, i.e. the denominator in formula (10)), and will always be using the ionospheric propagator in the form (16), (17) rather than (16), (26).

Replacing the non-dispersive propagator (7) with the dispersive propagator (16), (17), we obtain instead of formula (9),

$$\psi(t, \boldsymbol{x}) \approx \iiint_{|\boldsymbol{x}-z| \leqslant ct} \tilde{\nu}(\boldsymbol{x}, z) A'_{2\delta}(t - 2T_{\rm gr}(\boldsymbol{x}, z, \omega_0))\, \mathrm{e}^{\mathrm{i}\omega_0 (t - 2T_{\rm ph}(\boldsymbol{x}, z, \omega_0))}\, \mathrm{d}z, \tag{27}$$

where the notation $A'_{2\delta}$ indicates that the round trip effect on the chirp duration and rate is twice that of (23). Accordingly (see [6]), for the range and azimuthal factor of the GAF in the case of dispersive propagation, we have (cf formulae (14) and (15))

$$W'_R(\boldsymbol{y}, z) = \int \overline{A(t - 2|\boldsymbol{y} - \boldsymbol{x}^0|/c)} A'_{2\delta}(t - 2T_{\rm gr}(\boldsymbol{x}^0, z, \omega_0))\, \mathrm{d}t \tag{28}$$

and

$$W'_A(\boldsymbol{y}, z) = \sum_{n=-N/2}^{N/2} \mathrm{e}^{\frac{2\mathrm{i}\omega_0}{c}(|\boldsymbol{y} - \boldsymbol{x}^n| - cT_{\rm ph}(\boldsymbol{x}^n, z, \omega_0))}, \tag{29}$$

respectively.

2.2. Radar resolution and ionospheric distortions

Expression (28) for the range ambiguity function, accurate to a constant factor, is given by the following integral:

$$W'_R(\boldsymbol{y}, z) \propto \int_{\max\{-\tau/2 + 2R_y/c,\ -\tau''/2 + 2T_{\rm gr}(\boldsymbol{x}^0, z, \omega_0)\}}^{\min\{\tau/2 + 2R_y/c,\ \tau''/2 + 2T_{\rm gr}(\boldsymbol{x}^0, z, \omega_0)\}} \mathrm{e}^{\mathrm{i}(\alpha'' - \alpha)t^2}\, \mathrm{e}^{4\mathrm{i}(\alpha R_y/c - \alpha'' T_{\rm gr}(\boldsymbol{x}^0, z, \omega_0))t}\, \mathrm{d}t, \tag{30}$$

where (cf formula (23))

$$R_y = |\boldsymbol{x}^0 - \boldsymbol{y}|, \quad \tau'' = \tau - 2\delta\tau \quad \text{and} \quad \alpha'' = \alpha + 2\delta\alpha = \frac{B}{2\tau}\left(1 + \frac{2\delta\tau}{\tau}\right). \tag{31}$$

Changing the integration variable in (30) to $u = t - \left(\frac{R_y}{c} + T_{\rm gr}(\boldsymbol{x}^0, z, \omega_0)\right)$ and denoting

$$a = \alpha'' - \alpha \quad \text{and} \quad b = 2(\alpha + \alpha'')(R_y/c - T_{\rm gr}(\boldsymbol{x}^0, z, \omega_0)), \tag{32}$$

[4] In many ionospheric studies, the upper integration limit in (25) is formally taken as ∞.

we can convert integral (30) to

$$w(a,b) = \int_{-\tau/2}^{\tau/2} \exp(\mathrm{i}au^2 + \mathrm{i}bu)\,\mathrm{d}u. \tag{33}$$

Note that the exact integration limits are approximated by simpler expressions in (33), which introduces a small relative error $\sim \frac{\delta\tau}{\tau}$. A comprehensive analysis can be found in [35], where we consider all possible scenarios of how the intervals $\chi_\tau(t - 2|\boldsymbol{y} - \boldsymbol{x}^0|/c)$ and $\chi_{\tau''}(t - 2T_{\mathrm{gr}}(\boldsymbol{x}^0, z, \omega_0))$ can be positioned with respect to one another.

Integrals of type (33) commonly appear in the analysis of the radar ambiguity functions and their properties [36, 37]. The quadratic phase error (QPE) for (33) is defined as the maximum absolute value of the quadratic term in the exponent (see, e.g., [37, chapter 3.5] or [36, chapter 2.6]):

$$\phi_{\mathrm{q}} = |a|\left(\frac{\tau}{2}\right)^2. \tag{34}$$

The QPE characterizes the mismatch between the chirp rates in the direct (27) and inverse (11) operators that compose the GAF. If the QPE is small, then w of (33) can be represented as

$$w(a,b) \approx w_0(b) + w_1(a,b), \tag{35}$$

where

$$w_0(b) = \tau\,\mathrm{sinc}\left(\frac{b\tau}{2}\right) \equiv \tau\frac{\sin(b\tau/2)}{b\tau/2} \quad \text{and} \quad |w_1| \ll |w_0|. \tag{36}$$

With no dispersion at all, formula (32) yields $a = 0$ and $b = 4\alpha(R_y - R_z)/c$, because $T_{\mathrm{gr}} = R_z/c$. In this case, the semi-width of the main lobe of $w_0(b)$, which is given by the conditions $\frac{b\tau}{2} = \pm\pi$, determines the undistorted radar resolution in the range, $\Delta_R = \frac{\pi c}{B}$, see [1], while the sidelobes of w_0 determine the image contrast.

In the dispersive case, the term w_0 in (35) represents the effect of the filter with the group delay of the signal taken into account, but with no rate mismatch, i.e. no QPE. Substituting b of (32) into w_0 of (36) and keeping only the first term on the right-hand side of (35), we approximate (30) as follows:

$$W_R'(\boldsymbol{y}, z) \propto \tau\,\mathrm{sinc}([(\alpha'' + \alpha)R_y/c - (\alpha'' + \alpha)T_{\mathrm{gr}}(\boldsymbol{x}^0, z, \omega_0)]\tau). \tag{37}$$

The range resolution Δ_R is given by the semi-width of the main lobe of the sinc in (37). Setting $\frac{(\alpha''+\alpha)\Delta_R\tau}{c} = \pi$, we derive with the help of (31),

$$\Delta_R = \frac{\pi c}{B}\left(1 - \frac{\delta\tau}{\tau}\right). \tag{38}$$

Formula (38) yields roughly 19 m for the values of the parameters listed in table 1. The term $\frac{\delta\tau}{\tau}$ is formally kept in (38) only because it comes from the analysis of (37) with no simplifications. Otherwise, this term is small, about 0.15%, and of the same order as the terms dropped when simplifying the integration limits in (33). Thus, it can be neglected, and the range resolution in the dispersive case remains practically unchanged.

The term w_1 in (35) leads to the broadening of the main lobe of $w(a,b)$ and increase of its sidelobes, both of which add to the image blurring. Quantitatively, the role of w_1 has been estimated in [3, appendix C][5]. Specifically, it has been shown that at the edge of the main lobe, we have $|w| \neq 0$ due to the presence of w_1, so that

$$\frac{1}{\max|w|}|w|_{\frac{b\tau}{2}=\pi} \approx \frac{|w_1|_{\frac{b\tau}{2}=\pi}}{|w_0|_{\frac{b\tau}{2}=0}} \approx \frac{a\tau^2}{2\pi^2} = \frac{2}{\pi^2}\phi_{\mathrm{q}}, \tag{39}$$

[5] The effect of QPE can, to some degree, be controlled by introducing the weight functions into integral (11), see, e.g., [37]; we do not consider this approach here.

where the QPE ϕ_{q} is defined by (34) and should be small for (39) to hold. A non-zero value in (39) suggests that the image is smeared, because the main lobe is not so well defined compared to the case where $|w|_{\frac{b\tau}{2}=\pi} = 0$. For the typical parameters given in table 1, the extent of the smearing in the sense of (39) is $\sim 20\%$, assuming that for the definition of $\delta\tau$ in (23) we take $|\boldsymbol{x} - \boldsymbol{z}| \sim R$. An alternative measure for image imperfections due to the QPE is called the integrated side lobe ratio (ISLR). The ISLR is defined as a ratio of the power (i.e. integral of $|w|^2$) in the sidelobes to that in the main lobe, see [37, section 2.8]. It is usually expressed in decibels and can be calculated numerically. The increase of ISLR that corresponds to the data in table 1 is ~ 1.8 dB.

The ionosphere also causes a displacement of the image. Formula (36) indicates that w_0 attains its maximum at $b = 0$. In the non-dispersive case, we have $T_{\mathrm{gr}}(\boldsymbol{x}^0, \boldsymbol{z}, \omega_0) = R_z/c$ where $R_z = |\boldsymbol{x}^0 - \boldsymbol{z}|$, and according to (32), $b = 0$ for $R_y = R_z$. In other words, the sinc reaches its maximum value precisely when the reference location $\boldsymbol{y}$ and the target $\boldsymbol{z}$ are at the same distance away from the orbit in the normal direction. In the dispersive case though, $b = 0$ when $R_y = cT_{\mathrm{gr}}(\boldsymbol{x}^0, \boldsymbol{z}, \omega_0)$, where T_{gr} is given by (20). This is not equivalent to $R_y = R_z$, and hence the image of a point scatterer at $\boldsymbol{z}$ will be displaced in range with respect to its true position. The displacement is given by

$$S_R \stackrel{\mathrm{def}}{=} R_y - R_z = cT_{\mathrm{gr}}(\boldsymbol{x}^0, \boldsymbol{z}, \omega_0) - R_z = R_z \frac{1}{\omega_0^2} \frac{4\pi e^2}{2m_{\mathrm{e}}} \frac{N_H}{H} = \frac{1}{2} R_z \frac{\bar{\omega}_{\mathrm{pe}}^2}{\omega_0^2}. \tag{40}$$

For the parameters in table 1, formula (40) yields approximately 450 m, assuming that $R_z \approx R$. The origin of this displacement is the group delay, i.e. the mismatch between the actual propagation velocity $\bar{v}_{\mathrm{gr}}$ of (21), which is used in the direct operator (27), and the speed of light in the inverse operator (11). Although the displacement of the image in the range is a distortion *per se*, it appears of key importance for the reconstruction of the ionospheric TEC by means of dual-carrier probing (see section 4).

To analyze the azimuthal factor of the GAF, we first introduce the notation

$$\Psi_n = \frac{|\boldsymbol{y} - \boldsymbol{x}^n| - cT_{\mathrm{ph}}(\boldsymbol{x}^n, \boldsymbol{z}, \omega_0)}{R}, \tag{41}$$

so that the sum (29) is recast as

$$W_A'(\boldsymbol{y}, \boldsymbol{z}) = \sum_{n=-N/2}^{N/2} \mathrm{e}^{\frac{2i\omega_0 R}{c}\Psi_n}. \tag{42}$$

When calculating the distances in (41), we will use the subscripts '1' and '3' to denote the horizontal coordinates along the orbit (azimuth) and across the orbit (range), respectively, leaving the index '2' for the altitude, so that for the points on the orbit we will have $\boldsymbol{x} = (x_1, H, 0)$. For the target $\boldsymbol{z} = (z_1, 0, z_3)$, we will assume with no loss of generality that $z_1 = 0$, see figure 1; we also take $y_3 = z_3$ when analyzing azimuthal resolution. Then, we can linearize the travel distances:

$$\begin{aligned} R_z = |\boldsymbol{z} - \boldsymbol{x}| &= \sqrt{R^2 + (z_1 - x_1)^2} \approx R\left(1 + \frac{1}{2}\frac{x_1^2}{R^2}\right), \\ R_y = |\boldsymbol{y} - \boldsymbol{x}| &= \sqrt{R^2 + (y_1 - x_1)^2} \approx R\left(1 + \frac{1}{2}\frac{(y_1 - x_1)^2}{R^2}\right), \end{aligned} \tag{43}$$

because $|x_1^n| \ll R$ and $|y_1 - x_1^n| \ll R$, where $R = \sqrt{H^2 + z_3^2}$. Substituting (43) into (41), we obtain

$$\Psi_n = -\frac{y_1 x_1^n}{R^2} + \frac{\bar{\omega}_{\mathrm{pe}}^2}{\omega_0^2} \frac{(x_1^n)^2}{4R^2}. \tag{44}$$

For the azimuthal coordinate x_1 in formula (44) we can write: $x_1^n = n \cdot \Delta x_1$, where Δx_1 is the distance that the satellite travels along the orbit between the successive emission of pulses: $\Delta x_1 = v_{\mathrm{SAT}}/f_{\mathrm{p}}$. Introducing

$$\hat{a} = \frac{\omega_0 (\Delta x_1)^2}{2Rc} \frac{\bar{\omega}_{\mathrm{pe}}^2}{\omega_0^2} \quad \text{and} \quad \hat{b} = \frac{2\omega_0 y_1 \Delta x_1}{Rc}, \tag{45}$$

we can approximate the sum (42) by the integral:

$$W_A'(y_1, 0) \stackrel{\mathrm{def}}{=} W_A'(\boldsymbol{y}, \boldsymbol{z})\Big|_{\substack{z_1=0,\\ y_3=z_3}} = \sum_{n=-N/2}^{N/2} \mathrm{e}^{\mathrm{i}\hat{a}n^2 - \mathrm{i}\hat{b}n} \approx \int_{-N/2}^{N/2} \mathrm{e}^{\mathrm{i}\hat{a}n^2 - \mathrm{i}\hat{b}n}\, \mathrm{d}u. \tag{46}$$

The integral in (46) is of the type (33). Thus, the calculation of the azimuthal w_0 is equivalent to keeping only the first term on the right-hand side of (44) for the sum (42):

$$W_A'(y_1, 0) \approx \sum_{n=-N/2}^{N/2} \mathrm{e}^{-\frac{2\mathrm{i}\omega_0}{c} \frac{y_1 x_1^n}{R}} \approx N \operatorname{sinc} \frac{\omega_0 y_1 \Delta x_1 N}{Rc}. \tag{47}$$

The semi-width of the main lobe of the sinc in (47) yields the azimuthal resolution:

$$\Delta_A = \frac{1}{2} \frac{\lambda_0 R}{L_{\mathrm{SA}}}, \tag{48}$$

which appears approximately equal to 10 m for the typical parameters given in table 1.

The azimuthal w_1 is due to $\hat{a}$ of (45), i.e. to the second term on the right-hand side of (44). This second term accounts for the difference between the phase velocity in the dispersive propagator (17), (20) and the speed of light in the non-dispersive filter in (11). Similarly to (34), the expression for the azimuthal QPE is

$$\phi_{\mathrm{qA}} = \frac{\hat{a}N^2}{4} = \frac{1}{2} \frac{\omega_0}{Rc} \frac{\bar{\omega}_{\mathrm{pe}}^2}{\omega_0^2} \frac{1}{4} (N \Delta x_1)^2 = \frac{1}{8} \frac{\omega_0 L_{\mathrm{SA}}^2}{Rc} \frac{\bar{\omega}_{\mathrm{pe}}^2}{\omega_0^2}, \tag{49}$$

and the same argument that leads to equation (39) yields the deterioration of the GAF contrast of approximately 35% for the typical parameters given in table 1. Note though that such a substantial deterioration implies that the main lobe of the sinc absorbs the first sidelobe, the resolution drops and the measure of image defects based on formula (39) essentially loses its original meaning. On the other hand, the ISLR still provides an adequate measure, and the corresponding increase is about 4 dB.

3. Azimuthal displacement due to horizontal variation of the ionosphere

In section 2, we have assumed that the electron number density does not depend on the horizontal coordinates. Then, the only characteristic of the ionospheric plasma that enters the expression for the propagator (16) is the constant TEC given by (25).

In order to account for the horizontally inhomogeneous ionosphere, we will let the electron number density n_{e} depend not only on the altitude h but also on the azimuthal coordinate ξ_1. In doing so, we will assume that the dependence is predominantly linear and truncate the Taylor expansion of n_{e} in the direction ξ_1 after the second term:

$$n_{\mathrm{e}}(\xi_1, h) \approx n_{\mathrm{e}}(0, h) + \xi_1 \frac{\partial n_{\mathrm{e}}}{\partial \xi_1}(0, h), \quad \text{where} \quad |\xi_1| \ll R. \tag{50}$$

Following [6, appendix B], for $\omega^2 \gg \omega_{\rm pe}^2$ (see table 1) we can calculate the phase travel time by integrating the reciprocal phase velocity of (5) along the straight line connecting $\boldsymbol{x}$ and $\boldsymbol{z}$ (i.e. ignoring the ray curvature) (cf formulae (22) and (24)):

$$T_{\rm ph}(\boldsymbol{x},\boldsymbol{z},\omega) = \int_0^{R_z} \frac{{\rm d}s}{v_{\rm ph}(s)} = \frac{1}{\cos\theta}\int_0^H \frac{{\rm d}h}{v_{\rm ph}(\xi_1(h),h)} \approx \frac{R_z}{c} - \frac{1}{c\cos\theta}\int_0^H \frac{1}{2}\frac{\omega_{\rm pe}^2(\xi_1(h),h)}{\omega^2}\,{\rm d}h, \tag{51}$$

where $\xi_1(h)$ is the azimuthal coordinate of the point on the line between $\boldsymbol{x}$ and $\boldsymbol{z}$ that has altitude h (see figure 1):

$$\xi_1(h) \equiv \xi_1(\boldsymbol{x},\boldsymbol{z},h) = \frac{h}{H}x_1 + \frac{H-h}{H}z_1 = \frac{h}{H}x_1 \tag{52}$$

Substituting (52) into (51), we obtain

$$T_{\rm ph}(\boldsymbol{x},\boldsymbol{z},\omega) = \frac{R_z}{c} - \frac{1}{2c\omega^2\cos\theta}\int_0^H \left(\omega_{\rm pe}^2(0,h) + \frac{x_1}{H}\frac{4\pi e^2}{m_{\rm e}}\frac{\partial n_{\rm e}}{\partial\xi_1}(0,h)h\right){\rm d}h. \tag{53}$$

Then, using formulae (21)–(25), we transform expression (53) into

$$T_{\rm ph}(\boldsymbol{x},\boldsymbol{z},\omega) = \frac{R_z}{\bar v_{\rm ph}(\omega)} - \frac{R_z}{c}\frac{\bar\omega_{\rm pe}^2}{2\omega^2}Q(\boldsymbol{x}^0,\boldsymbol{z})x_1, \tag{54}$$

where

$$Q(\boldsymbol{x}^0,\boldsymbol{z}) \stackrel{\rm def}{=} \frac{1}{H^2}\int_0^H \frac{4\pi e^2}{m_{\rm e}\bar\omega_{\rm pe}^2}\frac{\partial n_{\rm e}}{\partial\xi_1}(0,h)h\,{\rm d}h \tag{55}$$

is essentially the first moment of the azimuthal gradient of $n_{\rm e}$. The quantities $\bar\omega_{\rm pe}^2$ and $\bar v_{\rm ph}(\omega)$ in formulae (54) and (55) are evaluated according to (24) and (21), respectively, for $\xi_1 = 0$, i.e. for $\omega_{\rm pe}^2 = \omega_{\rm pe}^2(0,h) \;\Leftrightarrow\; n_{\rm e} = n_{\rm e}(0,h)$. Substituting (55), (54) and (43) into (41), we have (cf formula (44))

$$\Psi_n = -\frac{y_1 x_1^n}{R^2} + \frac{\bar\omega_{\rm pe}^2}{\omega_0^2}\frac{(x_1^n)^2}{4R^2} + \frac{\bar\omega_{\rm pe}^2}{2\omega_0^2}Qx_1. \tag{56}$$

With the third term on the right-hand side of (56) taken into account, and the second term temporarily disregarded, we obtain instead of formula (47):

$$W_A'(y_1,0) \approx \sum_{n=-N/2}^{N/2} {\rm e}^{-\frac{2{\rm i}\omega_0}{c}\left(\frac{y_1}{R} - R\frac{\bar\omega_{\rm pe}^2}{2\omega_0^2}Q\right)x_1^n} \approx N\,{\rm sinc}\left[\frac{\omega_0}{c}\left(\frac{y_1}{R} - R\frac{\bar\omega_{\rm pe}^2}{2\omega_0^2}Q\right)\Delta x_1 N\right].$$

Consequently, a non-zero value of Q of (55), which is due to the azimuthal gradient of $n_{\rm e}$, see (50), results in an azimuthal displacement of the entire image by

$$S_A = \frac{1}{2}\frac{\bar\omega_{\rm pe}^2}{\omega_0^2}QR^2. \tag{57}$$

As in the case of the displacement in range, see formula (40), the origin of the azimuthal displacement (57) is a mismatch between the filter in (11) and the propagator (17). The presence of the azimuthal displacement (57) allows us to reconstruct the value of Q by means of the dual-carrier probing (see section 4) and subsequently use this value to correct the matched filter in (11).

The effect of the second term on the right-hand side of (56) is exactly the same for the horizontally inhomogeneous ionosphere as it is for the horizontally homogeneous ionosphere. Namely, the QPE leads to a deterioration of the GAF contrast, see (49).

It is also to be noted that in the literature one sometimes uses a simplified model based on the so-called phase screens to describe the propagation of radar pulses through the ionosphere, see, e.g., [23, 38, 13].

4. Robust evaluation of ionospheric parameters by dual-carrier probing

In the previous sections, it has been demonstrated how mismatches between the direct and inverse operators (formulae (27) and (11), respectively) result in image distortions of various kinds. For a horizontally homogeneous ionosphere (section 2.2), these mismatches include a substantial displacement of the entire image in range, as well as both range and azimuthal smearing. Horizontal inhomogeneity of the ionosphere (section 3) adds an azimuthal displacement that may sometimes be of the same magnitude as the range displacement. Our goal is to remove (or reduce) the mismatches and thus reduce the image distortions. The mismatches originate from the difference between the actual phase and group travel times of radar signals in the ionosphere (formulae (16)–(23)) and the expression $|\boldsymbol{x} - z|/c$ in (11) that is based on the speed of light in vacuum. Hence, it is necessary to evaluate the parameters of the ionospheric plasma that appear in formulae (21), (24) and (54). It is important to note that in order to correct the image, we need to know these parameters at the actual time and place of the image acquisition, as opposed to knowing the statistically averaged values.

The approach to correcting the ionospheric distortions based on dual-carrier probing assumes that at the first stage, two SAR images of the same area at the same time are acquired using two different carrier frequencies and a filter with no correction. Each of the two images will be displaced from the ground truth, but the magnitude of the displacement will depend on the carrier frequency, see (40). In doing so, the difference between the two values of the displacement allows one to estimate the parameter $\bar{\omega}_{\rm pe}^2$ given by (24). Then, $\bar{\omega}_{\rm pe}^2$ is substituted into formulae (21), which helps determine the phase and group travel times (20) and the new chirp rate and length (23). These quantities, in turn, are used to build a new filter $\overline{P'}$ based on (17) that would match the actual signal that propagates through the ionosphere (16). The distortions of the image obtained with the help of the new filter will be reduced or removed.

Following [6], we assume that there exists a point-like object in the scene that is imaged at two different slant distances $R_y^{(1)}$ and $R_y^{(2)}$ using carrier frequencies ω_1 and ω_2. Then, formula (40) yields two equations for $\bar{\omega}_{\rm pe}^2$ and the true distance to the object R_z:

$$\begin{aligned} R_y^{(1)} &= cT_{\rm gr}(\boldsymbol{x}^0, z, \omega_1) = R_z\left(1 + \frac{\bar{\omega}_{\rm pe}^2}{2\omega_1^2}\right), \\ R_y^{(2)} &= cT_{\rm gr}(\boldsymbol{x}^0, z, \omega_2) = R_z\left(1 + \frac{\bar{\omega}_{\rm pe}^2}{2\omega_2^2}\right). \end{aligned} \tag{58}$$

Solving system (58) with respect to $\bar{\omega}_{\rm pe}^2$, we obtain

$$\bar{\omega}_{\rm pe}^2 = \frac{2\omega_1^2\omega_2^2\Delta R_y}{\omega_2^2 R_y^{(2)} - \omega_1^2 R_y^{(1)}}, \quad \text{where} \quad \Delta R_y \equiv R_y^{(1)} - R_y^{(2)}. \tag{59}$$

A similar approach can be used to reconstruct the horizontal inhomogeneity parameter Q from the measurements of the azimuthal displacement S_A on two images. According to (57), the azimuthal coordinates $y_1^{(1)}$ and $y_1^{(2)}$ of a given object on two images are related to its true azimuthal coordinate z_1 by

$$\begin{aligned} y_1^{(1)} &= z_1 + \frac{1}{2}\frac{\bar{\omega}_{\rm pe}^2}{\omega_1^2} QR^2, \\ y_1^{(2)} &= z_1 + \frac{1}{2}\frac{\bar{\omega}_{\rm pe}^2}{\omega_2^2} QR^2, \end{aligned}$$

which yields

$$\bar{\omega}_{\rm pe}^2 QR^2 = \frac{2\omega_1^2\omega_2^2\Delta y_1}{\omega_2^2 - \omega_1^2}, \quad \text{where} \quad \Delta y_1 \equiv y_1^{(1)} - y_1^{(2)}. \tag{60}$$

Formulae (59) and (60) allow one to reconstruct the ionospheric parameters $\bar{\omega}_{\rm pe}^2$ and Q that are responsible for the filter mismatch between $\overline{P}$ in (11) and P' in (17). The deficiencies of this method include the following.

(i) Formula (59) involves a small quantity $\Delta R_y = R_y^{(1)} - R_y^{(2)}$ defined as a difference of two large quantities. Hence, this formula is poorly conditioned, i.e. sensitive to errors in the input data $R_y^{(1)}$ and $R_y^{(2)}$, see [6].

(ii) The method of (58)–(59) requires having point-like objects in the scene. Yet the initial images built using the uncorrected filter may be smeared because of the chirp rate mismatches (section 2.2). With no sharp objects, the measurements of $R_y^{(1)}$ and $R_y^{(2)}$ should use diffuse objects and/or brightness gradients, which reduces the accuracy and further aggravates the problem outlined in item (i). Additional complication comes from the fact that the extent of smearing depends on the radar frequency, and thus one and the same object may appear different in two images.

(iii) Expression (59) yields a single value of $\bar{\omega}_{\rm pe}^2$, whereas the electron number density may, in fact, vary over the scale of the image, so that different values of the TEC may be needed for different parts of the image.

Paper [6] addresses the issue of conditioning of formula (59) by exploiting multiple pairs of $(R_y^{(1)}, R_y^{(2)})$ chosen over the image, so that the result given by (59) is averaged over the set of those pairs. If the values of $\bar{\omega}_{\rm pe}^2$ obtained for individual pairs are interpreted as independent random variables, then this approach may reduce the total error by a factor of $\sqrt{L}$, where L is the number of pairs. It, however, puts an even higher demand on the availability of sharp objects (item (ii)), whereas if the TEC varies over the image (item (iii)), there will be little or no improvement.

In the current work, instead of determining the range values R_y from individual images, we propose to calculate the shift between the two images using registration techniques [25]. The key advantage of the registration approach is that it determines the value of ΔR_y directly, as opposed to computing it as the difference of two much larger values. While there is still a need to know $R_y^{(1)}$ and $R_y^{(2)}$ individually to calculate the denominator in (59), it has been shown in [6] that it is the quantity ΔR_y in the numerator of (59) that is primarily responsible for the poor conditioning of the formula.

A particular registration method that can be used is known as phase correlation [31, 32]. It belongs to the family of area-based image registration techniques [25][6]. Consider two functions of a single real argument: $u(x)$ and $v(x) \equiv u(x - s)$, where s is the unknown shift. Then, for the Fourier transforms of u and v we have

$$\hat{u}(\kappa) = \int_{-\infty}^{\infty} u(x)\, \mathrm{e}^{-\mathrm{i}\kappa x}\, \mathrm{d}x \quad \Rightarrow \quad \hat{v}(\kappa) = \int_{-\infty}^{\infty} u(x-s)\, \mathrm{e}^{-\mathrm{i}\kappa x}\, \mathrm{d}x = \mathrm{e}^{-\mathrm{i}\kappa s}\hat{u}(\kappa). \tag{61}$$

Therefore,

$$\tilde{\delta}(x) \stackrel{\rm def}{=} \int_{-\infty}^{\infty} \frac{\hat{u}^*(\kappa)\hat{v}(\kappa)}{|\hat{u}^*(\kappa)\hat{v}(\kappa)|}\, \mathrm{e}^{\mathrm{i}\kappa x}\, \mathrm{d}\kappa = \int_{-\infty}^{\infty} \mathrm{e}^{-\mathrm{i}\kappa s}\, \mathrm{e}^{\mathrm{i}\kappa x}\, \mathrm{d}\kappa = 2\pi\delta(x-s), \tag{62}$$

where asterisk (*) denotes complex conjugation. The idea of phase correlation for the area-based image registration is to look for the value of x that delivers the maximum to $\tilde{\delta}(x)$ of (62). In the ideal world, $\tilde{\delta}(x)$ peaks exactly at s, so the approach immediately yields the shift. Moreover, one can interpret the shift obtained this way as an independent quantity rather than the difference ΔR_y of two large distances, as in the original formula (59). In the real world, one uses a discrete Fourier transform instead of both (61) and (62). This leads to the

[6] The technique of [6], which exploits multiple objects, is an example of feature-based registration.

usual ambiguities due to the finite size of the image and finite size of the grid, on which the discrete transform is done, and the result is no longer a pure δ-function. It is rather a grid function with its maximum at the node closest to $x = s$, see appendix C. This brings the accuracy of determining the shift s to half the grid size, which has a lower bound of half the pixel size. Additional steps can be taken to improve this accuracy further, and also to mitigate the component of the error due to the presence of noise, see [39]. Altogether, the error of determining the shift s by phase correlation decreases as $L^{-1/2}$, see formula (C.8), where L is the dimension of the discrete Fourier transform[7]. It is fundamentally the same 'inverse square root' behavior as appears in the feature-based registration. The advantage of the area-based approach is that by involving areas without distinct point-like features it helps increase the effective number of 'pairs of the reference points,' and thus improves the accuracy and robustness of the shift estimation. In practice, the best techniques currently available in the literature report the accuracy of the area-based image registration of only a few per cent of the resolution cell, see [26–30].

We note that the functions $u(x)$ and $v(x)$ in formula (61), as well as in appendix C, represent the absolute value of the complex image $I(\boldsymbol{y})$. Correlation of complex images, called coherent cross correlation in [40], provides a better registration accuracy, but is only possible if frequency bands of the two images substantially overlap.

In section 5, we show how the accuracy of registration affects the accuracy of TEC reconstruction by dual-carrier probing. We also analyze the residual distortions of SAR images. When making numerical estimates, we will assume that the registration accuracy, in both range and azimuthal directions, is 5% of the corresponding resolution.

5. Performance of the matched filter with ionospheric corrections

5.1. Implementation of ionospheric corrections into the matched filter

Let us recall that the goal of reconstructing the parameters of the ionosphere $\bar{\omega}_{\rm pe}^2$ and Q is to correct formula (11) (as well as formulae (12) and (13)), i.e. replace the filter $\overline{P(\boldsymbol{x}, \boldsymbol{y}, \omega_0)}$ by the complex conjugate of $P'(\boldsymbol{x}, \boldsymbol{y}, \omega_0)$ of (17), so that the mismatch between the filter and the dispersive propagator is removed. If $\bar{\omega}_{\rm pe}^2$ is known, then P' can be obtained by evaluating the travel times $T_{\rm ph}(\boldsymbol{x}^n, \boldsymbol{y}, \omega_0)$ and $T_{\rm gr}(\boldsymbol{x}^n, \boldsymbol{y}, \omega_0)$ with the help of formulae (20) and (21), and also computing corrections to the chirp rate and duration using (23). Furthermore, if Q is known, then an additional correction to the phase travel time is given by formula (54), and a similar formula can be easily derived for the group travel time by flipping the sign in front of Q and replacing $\bar{v}_{\rm ph}$ by $\bar{v}_{\rm gr}$.

The ionospheric parameters $\bar{\omega}_{\rm pe}^2$ and Q are reconstructed using the dual-carrier approach of section 4, i.e. by means of formulae (59) and (60). The values of $\Delta R_{\boldsymbol{y}}$ and Δy_1 entering these formulae are obtained by evaluating the shift between the two SAR images with the help of image registration (see section 4 and appendix C). In doing so, the accuracy of reconstructing $\bar{\omega}_{\rm pe}^2$ and Q will obviously depend on the accuracy of registration. The latter is discussed in appendix C, and for the rest of this section we will analyze the effect of the registration errors on the performance of the corrected matched filter. In [6], we have conducted similar analysis for horizontally homogeneous ionosphere, and under the assumption that the TEC is reconstructed exactly.

[7] The value of L may not exceed the overall number of pixels in a given direction, see appendix C.

5.2. Residual errors of corrected filter

Throughout this section, we are using the tilde above a symbol (e.g., $\tilde{\omega}_{\rm pe}^2$, $\tilde{\alpha}$, $\tilde{W}_R$) to denote the quantities computed with the help of the reconstructed TEC.

5.2.1. Range factor. The analysis of the range factor of the GAF will be based on formula (28) with the replacement

$$\overline{A(t-2|\boldsymbol{y}-\boldsymbol{x}^0|/c)} \mapsto \overline{A_{2\delta}(t-2|\boldsymbol{y}-\boldsymbol{x}^0|/\tilde{v}_{\rm gr})}, \quad \text{where} \quad \tilde{v}_{\rm gr} = c\left(1-\frac{1}{2}\frac{\tilde{\omega}_{\rm pe}^2}{\omega_0^2}\right).$$

Note that the quantity Q does not contribute to $\tilde{T}_{\rm gr}(\boldsymbol{x}^0,\boldsymbol{y},\omega_0)$ because $x_1^0 = 0$, so that $\tilde{T}_{\rm gr}(\boldsymbol{x}^0,\boldsymbol{y},\omega_0) = |\boldsymbol{y}-\boldsymbol{x}^0|/\tilde{v}_{\rm gr}(\omega_0)$ (cf formula (54)). Changing the integration variable from t to $u = t - \big(\tilde{T}_{\rm gr}(\boldsymbol{x}^0,\boldsymbol{y},\omega_0) + T_{\rm gr}(\boldsymbol{x}^0,\boldsymbol{z},\omega_0)\big)$, we obtain (similar to obtaining (33) from (30))

$$\tilde{W}_R(\boldsymbol{y},\boldsymbol{z}) \propto \int_{-\tilde{\tau}/2}^{\tilde{\tau}/2} \mathrm{e}^{\mathrm{i}\tilde{a}u^2+\mathrm{i}\tilde{b}u}\,\mathrm{d}u, \tag{63}$$

where (cf formulae (23), (31) and (32))

$$\tilde{\tau} = \tau - 2\delta\tilde{\tau}(\boldsymbol{y}) = \tau - 2\frac{|\boldsymbol{y}-\boldsymbol{x}^0|}{c}\frac{\tilde{\omega}_{\rm pe}^2}{\omega_0^2}\frac{B}{\omega_0}, \quad \tilde{\alpha} = \alpha + 2\delta\tilde{\alpha}(\boldsymbol{y}) = \alpha + 2\frac{\delta\tilde{\tau}}{2}\frac{B}{\tau^2},$$
$$\tilde{a} = \alpha'' - \tilde{\alpha}, \quad \text{and} \quad \tilde{b} = \tilde{b}(\boldsymbol{y},\boldsymbol{z}) = 2(\alpha''+\alpha)\left(\frac{|\boldsymbol{y}-\boldsymbol{x}^0|}{\tilde{v}_{\rm gr}} - \frac{|\boldsymbol{z}-\boldsymbol{x}^0|}{\tilde{v}_{\rm gr}}\right). \tag{64}$$

As in section 2.2, we first disregard the QPE under the integral in (63), in which case it approximately evaluates to (cf formula (36))

$$\tilde{W}_R(\boldsymbol{y},\boldsymbol{z}) \propto \tilde{\tau}\,\mathrm{sinc}\Big(\frac{\tilde{b}\tilde{\tau}}{2}\Big). \tag{65}$$

From (65) and (64), we obtain the new overall displacement of the image in the range

$$\tilde{S}_R = R_y - R_z \approx R_z\frac{1}{2}\frac{\bar{\omega}_{\rm pe}^2 - \tilde{\omega}_{\rm pe}^2}{\omega_0^2}, \tag{66}$$

where $R_y = |\boldsymbol{y}-\boldsymbol{x}^0|$ and $R_z = |\boldsymbol{z}-\boldsymbol{x}^0|$ as before. Formula (66) shows that the displacement $\tilde{S}_R$ is directly proportional to the error of the reconstructed TEC. The two 'extreme' cases here are no correction at all, i.e. no attempt to reconstruct the TEC, and the exact reconstruction of the TEC. If no filter correction is implemented, then one can set $\tilde{\omega}_{\rm pe}^2 = 0$ and formula (66) reduces to (40), whereas if the TEC is reconstructed exactly, then $\tilde{\omega}_{\rm pe}^2 = \bar{\omega}_{\rm pe}^2$ and $\tilde{S}_R = 0$, which is a result from [6].

To derive the new range resolution from (65) and (64), we set $\frac{(\alpha''+\alpha)\tilde{\Delta}_R\tilde{\tau}}{\tilde{v}_{\rm gr}} = \pi$ and obtain

$$\tilde{\Delta}_R \approx \frac{\pi c}{B}\left(1-\frac{(\delta\tau-\delta\tilde{\tau})}{\tau}\right)\left(1-\frac{1}{2}\frac{\tilde{\omega}_{\rm pe}^2}{\omega_0^2}\right). \tag{67}$$

Again, with no correction $\tilde{\omega}_{\rm pe}^2 = 0$ and $\delta\tilde{\tau} = 0$, so that formula (67) reduces to (38).

To obtain quantitative estimates for (66) and (67), we need to relate the accuracy of reconstructing the TEC to the accuracy of registering the two images, i.e. accuracy of obtaining the shift ΔR_y (section 4 and appendix C). Let us denote by $\delta(\bar{\omega}_{\rm pe}^2)$ and $\delta(\Delta R_y)$ the errors in determining $\bar{\omega}_{\rm pe}^2$ and ΔR_y, respectively. Then, according to (59) we can write

$$\delta(\bar{\omega}_{\rm pe}^2) \stackrel{\rm def}{=} \bar{\omega}_{\rm pe}^2 - \tilde{\omega}_{\rm pe}^2 \approx \frac{2\omega_1^2\omega_2^2\delta(\Delta R_y)}{\omega_2^2 R_y^{(2)} - \omega_1^2 R_y^{(1)}}. \tag{68}$$

In turn, the error in evaluating the shift ΔR_y can be taken as a fraction of the undistorted range resolution or, equivalently, a fraction of the pixel size (see appendix C)

$$\delta(\Delta R_y) \stackrel{\text{def}}{=} \zeta_R \frac{\pi c}{B}. \tag{69}$$

Hence, combining formulae (66), (68) and (69), we can write

$$\tilde{S}_R \approx R_z \frac{\omega_2^2}{\omega_2^2 R_y^{(2)} - \omega_1^2 R_y^{(1)}} \zeta_R \frac{\pi c}{B}, \tag{70}$$

where we have identified the central carrier frequency ω_0 with one of the two carrier frequencies used for dual-carrier probing, namely, ω_1[8]. Next, let us introduce the carrier frequency separation factor

$$Z \stackrel{\text{def}}{=} \frac{|\omega_2 - \omega_1|}{\omega_1}, \tag{71}$$

and assume that $Z \ll 1$, which also implies $\frac{\omega_2+\omega_1}{\omega_1} \approx 2$. Then, given that $R_z \approx R_y^{(1)} \approx R_y^{(2)} \approx R$, formula (70) yields

$$\tilde{S}_R \approx \frac{\zeta_R}{2Z} \frac{\pi c}{B}. \tag{72}$$

Remarkably, this estimate of the residual displacement given as a fraction of the range resolution $\frac{\pi c}{B}$ does not depend on the TEC. If, for example, $Z = 10\%$ ($\omega_1/2\pi = 300$ MHz as in table 1 and $\omega_2/2\pi = 330$ MHz), and the dimensionless factor $\zeta_R = 0.05 = 5\%$, which is reasonable for sub-pixel registration, then formula (72) yields $\tilde{S}_R \approx 5.5$ m. This is a most notable improvement over $S_R \approx 450$ m given by formula (40). In other words, with the filter correction in effect the displacement of the image in range is practically removed. As for the range resolution (67), it shows little change compared to either (38) or the undistorted value $\frac{\pi c}{B}$.

What the correction of the filter helps improve very substantially is the contrast/sharpness of the GAF. The corresponding estimate is given by formula (39) with the following QPE (see (31), (34), (64), (66) and (72)):

$$\begin{aligned}\tilde{\phi}_{\text{q}} &= |\tilde{a}|\frac{\tilde{\tau}^2}{4} = |\alpha'' - \tilde{\alpha}|\frac{\tilde{\tau}^2}{4} = 2|\delta\alpha - \delta\tilde{\alpha}|\frac{\tilde{\tau}^2}{4} = 2\alpha\frac{|\delta\alpha - \delta\tilde{\alpha}|}{\alpha}\frac{\tilde{\tau}^2}{4} = \frac{B}{\tau}\frac{|\delta\tau - \delta\tilde{\tau}|}{\tau}\frac{\tilde{\tau}^2}{4} \\ &\approx \frac{B}{\tau^2}\frac{R}{c}\left|\frac{\tilde{\omega}_{\text{pe}}^2}{\omega_0^2} - \frac{\tilde{\omega}_{\text{pe}}^2}{\omega_0^2}\right|\frac{B}{\omega_0}\frac{\tilde{\tau}^2}{4} \approx \frac{B}{\tau^2}\frac{R}{c}\left|\frac{2\tilde{S}_R}{R}\right|\frac{B}{\omega_0}\frac{\tilde{\tau}^2}{4} = \frac{B}{\tau^2 c}2\frac{\zeta_R}{2Z}\frac{\pi c}{B}\frac{B}{\omega_0}\frac{\tilde{\tau}^2}{4} \approx \frac{\zeta_R}{4Z}\frac{\pi B}{\omega_0},\end{aligned}$$

which yields only about 0.2% of contrast deterioration for the parameters in table 1, as opposed to 20% in the non-corrected case (39). If the TEC is reconstructed exactly, then the correction yields about four orders of magnitude of improvement, see [6].

Remark. Another way of comparing the initial shift and the residual shift (formulae (40) and (72), respectively) is to determine the TEC sensitivity, i.e. the minimal value of the TEC for which the correction is still beneficial. The carrier frequency separation factor Z in (72) cannot be made very large because of the technical limitations. In appendix D, we analyze the extreme situation where the separation of carrier frequencies is capped by the single bandwidth. This is called a split bandwidth configuration. The analysis shows that in this case, the formulae for the residual shift and the TEC sensitivity have an inverse square dependence on the system bandwidth, see (D.4) and (D.5), as opposed to the inverse dependence on the bandwidth in (72).

[8] In fact, ω_0 can be identified either with ω_1 or with ω_2.

5.2.2. Azimuthal factor. The azimuthal factor of the GAF $\tilde{W}_A(\boldsymbol{y}, z)$ with the corrected filter will still be given by formula (42), where instead of (41) we substitute

$$\tilde{\Psi}_n = \frac{c(\tilde{T}_{\rm ph}(\boldsymbol{x}^n, \boldsymbol{y}, \omega_0) - T_{\rm ph}(\boldsymbol{x}^n, z, \omega_0))}{R}. \tag{73}$$

Then, using formulae (21), (43) and (54) we can write

$$\begin{aligned}\tilde{\Psi}_n \approx & \left(1 + \frac{(y_1 - x_1^n)^2}{2R^2}\right)\left(1 - \frac{1}{2}\frac{\tilde{\omega}_{\rm pe}^2}{\omega_0^2}[1 + \tilde{Q}(x_1^n - y_1)]\right) \\ & - \left(1 + \frac{(x_1^n)^2}{2R^2}\right)\left(1 - \frac{1}{2}\frac{\bar{\omega}_{\rm pe}^2}{\omega_0^2}(1 + Qx_1^n)\right) \\ \approx & -\frac{y_1 x_1^n}{R^2}\left(1 - \frac{1}{2}\frac{\tilde{\omega}_{\rm pe}^2}{\omega_0^2}\right) + \frac{\bar{\omega}_{\rm pe}^2 - \tilde{\omega}_{\rm pe}^2}{\omega_0^2}\frac{(x_1^n)^2}{4R^2} + \frac{\bar{\omega}_{\rm pe}^2 Q - \tilde{\omega}_{\rm pe}^2\tilde{Q}}{2\omega_0^2}x_1^n + \text{const},\end{aligned} \tag{74}$$

where we have dropped the small term $\frac{1}{2}\frac{\tilde{\omega}_{\rm pe}^2}{\omega_0^2}\frac{y_1 x_1^n}{R^2}\tilde{Q}(x_1^n - y_1)$, as well as all the terms $\sim (x_1^n)^3$, which are also small. The first term on the last line of (74) corresponds to the first term on the right-hand side of (56), whereas the second and third terms show the effect of the corrected filter on the azimuthal QPE and azimuthal displacement of the image, respectively. The term 'const' combines everything that does not depend on n.

To evaluate the azimuthal displacement for the corrected filter using formula (74), we first introduce the dimensionless registration accuracy ζ_A as a fraction of the undistorted azimuthal resolution (48) (cf formula (69)):

$$\delta(\Delta y_1) \stackrel{\rm def}{=} \zeta_A \Delta_A = \zeta_A \frac{R}{2}\frac{\lambda}{L_{\rm SA}}. \tag{75}$$

Then, the error of reconstructing the quantity $\bar{\omega}_{\rm pe}^2 Q$ can be obtained from formula (60) with the help of formulae (75) and (71):

$$\delta(\bar{\omega}_{\rm pe}^2 Q) \stackrel{\rm def}{=} \bar{\omega}_{\rm pe}^2 Q - \tilde{\omega}_{\rm pe}^2\tilde{Q} \approx \frac{1}{R^2}\frac{\omega_1^2\omega_2^2}{\omega_2^2 - \omega_1^2}\zeta_A R\frac{\lambda}{L_{\rm SA}} \approx \frac{\zeta_A}{2Z}\omega_0^2\frac{\lambda}{RL_{\rm SA}}. \tag{76}$$

Formula (76), combined with (42) and (74), yields the residual azimuthal displacement of the image in the case of a corrected filter (cf formula (57)):

$$\tilde{S}_A = \frac{1}{2}R^2\frac{\delta(\bar{\omega}_{\rm pe}^2 Q)}{\omega_0^2} = \frac{\zeta_A}{2Z}\frac{R}{2}\frac{\lambda}{L_{\rm SA}}, \tag{77}$$

which is approximately 2.5 m for the typical parameters given in table 1. Note that formulae (72) and (77) are similar in the sense that both use the factors $\zeta_{R,A}/(2Z)$ to relate the residual displacement of the image $\tilde{S}_R$ and $\tilde{S}_A$ to the range and azimuthal resolutions given by formulae (38) and (48), respectively.

Similar to the range resolution (67), the new azimuthal resolution obtained with the help of formulae (42) and (74)

$$\tilde{\Delta}_A = \frac{1}{2}\frac{\lambda_0 R}{L_{\rm SA}}\left(1 + \frac{1}{2}\frac{\tilde{\omega}_{\rm pe}^2}{\omega_0^2}\right)$$

shows little change after the correction of the filter (i.e. little change compared to (48)). Yet the GAF contrast in the azimuthal direction improves very substantially. Indeed, the new value of the parameter $\hat{a}$ (see formulae (45) and (46)) due to the second term on the last line of (74) differs from the one that corresponds to (44) (or (56)) by a factor of $\delta(\bar{\omega}_{\rm pe}^2)/\bar{\omega}_{\rm pe}^2$. Hence, the

same will be the reduction of the azimuthal QPE, and using formulae (68), (69) and (49) we obtain

$$\tilde{\phi}_{\mathrm{qA}} = \phi_{\mathrm{qA}} \frac{\delta(\bar{\omega}_{\mathrm{pe}}^2)}{\bar{\omega}_{\mathrm{pe}}^2} = \frac{\zeta_R}{8Z} \frac{\pi \omega_0 L_{\mathrm{SA}}^2}{R^2 B}. \tag{78}$$

Expression (78) leads to only about 0.4% of deterioration of the GAF contrast in azimuth, as opposed to 35% given by formula (49).

6. The effect of ionospheric turbulence

In our previous analysis we have assumed that the electron number density in the ionosphere was a regular function of the altitude h and, maybe, the horizontal coordinate x_1: $n_{\mathrm{e}} = n_{\mathrm{e}}(x_1, h)$; see sections 2 and 3, as well as appendix A and appendix B. The actual Earth's ionosphere, however, is a turbulent medium. To characterize the ionospheric turbulence, we write the electron number density as follows:

$$n_{\mathrm{e}} = \langle n_{\mathrm{e}} \rangle + \mu(\boldsymbol{x}), \tag{79}$$

where $\langle n_{\mathrm{e}} \rangle$ is the mean value and μ represents the fluctuations $\langle \mu \rangle = 0$. If $\langle n_{\mathrm{e}} \rangle$ were constant, then we could assume that $\mu(\boldsymbol{x})$ was a homogeneous and isotropic random field, with the correlation function that depends only on the distance $r = |\boldsymbol{x}_1 - \boldsymbol{x}_2|$ rather than on the individual locations $\boldsymbol{x}_1 \in \mathbb{R}^3$ and $\boldsymbol{x}_2 \in \mathbb{R}^3$:

$$V(\boldsymbol{x}_1, \boldsymbol{x}_2) \stackrel{\mathrm{def}}{=} \langle \mu(\boldsymbol{x}_1)\mu(\boldsymbol{x}_2) \rangle = V(|\boldsymbol{x}_1 - \boldsymbol{x}_2|) \equiv V(r). \tag{80}$$

In reality, though, $\langle n_{\mathrm{e}} \rangle$ is a function of x_1 and h. At the same time, the ratio

$$M = \frac{\sqrt{\langle \mu^2 \rangle}}{\langle n_{\mathrm{e}} \rangle} \tag{81}$$

is assumed to be constant. A typical numerical value of M is 5×10^{-3}, and in extreme situations it may reach 10^{-1} [41]. Hence, $\sqrt{\langle \mu^2 \rangle}$ also depends on x_1 and h, which makes $\mu(\boldsymbol{x})$ a quasi-homogeneous (rather than truly homogeneous) random field. While in this case we keep the same notation (80) for the correlation function, in fact we have $V = V(x_1, h, r)$, where the dependence on x_1 and h is slow, and the dependence on r is fast.

For the Kolmogorov–Obukhov turbulence, the spectrum is (see [42, section 12.1])

$$\hat{V}(q) = \frac{C}{(1 + q^2/q_0^2)^{\kappa}}, \quad \text{where} \quad \kappa = \frac{11}{6} \ \text{ and } \ C = \text{const}. \tag{82}$$

Hence, the correlation function evaluates to

$$\begin{aligned} V(r) &\stackrel{\mathrm{def}}{=} \iiint_{-\infty}^{\infty} \hat{V}(\boldsymbol{q})\, \mathrm{e}^{\mathrm{i}\boldsymbol{q}\boldsymbol{r}}\, \mathrm{d}\boldsymbol{q} = 4\pi \int_0^{\infty} \frac{\sin qr}{qr} \hat{V}(q) q^2\, \mathrm{d}q \\ &= \frac{1}{\Gamma(\kappa)} 2^{\frac{5}{2}-\kappa} C \pi^{\frac{3}{2}} q_0^{\frac{3}{2}+\kappa} r^{-\frac{3}{2}+\kappa} K_{\kappa-\frac{3}{2}}(q_0 r), \end{aligned} \tag{83}$$

where $K_{\kappa-\frac{3}{2}}$ is the Macdonald function, or modified Bessel function of the second kind (see, e.g., [43, chapter VII, section 3]). Asymptotically for large r, we have $K_{\kappa-\frac{3}{2}}(q_0 r) \approx \sqrt{\frac{\pi}{2q_0 r}}\, \mathrm{e}^{-q_0 r}$, so that the correlation function decays exponentially:

$$V(r) \approx \frac{2^{2-\kappa}}{\Gamma(\kappa)} C \pi^2 \left(\frac{q_0}{r}\right)^{\frac{3}{2}} (q_0 r)^{\kappa-\frac{1}{2}}\, \mathrm{e}^{-q_0 r}. \tag{84}$$

This means that effectively we are taking into account only short-range phenomena in the ionosphere. The quantity q_0 in formulae (82)–(84) helps define the correlation length r_0, or the outer scale of turbulence:

$$r_0 \stackrel{\text{def}}{=} \frac{1}{V(0)}\int_0^\infty V(r)\,\mathrm{d}r = \left(C\pi^{\frac{3}{2}}\frac{\Gamma(\kappa-\frac{3}{2})}{\Gamma(\kappa)}q_0^3\right)^{-1}\frac{C\pi^2 q_0^2}{\kappa-1} = \frac{\sqrt{\pi}\Gamma(\kappa)}{(\kappa-1)\Gamma(\kappa-\frac{3}{2})}\frac{1}{q_0}, \tag{85}$$

where we have taken into account that

$$V(0) = \iiint_{-\infty}^{\infty}\hat{V}(\boldsymbol{q})\,\mathrm{d}\boldsymbol{q} = \int_0^\infty\int_0^{2\pi}\int_0^\pi V(q)q^2\sin\theta\,\mathrm{d}\theta\,\mathrm{d}\phi\,\mathrm{d}q = C\pi^{3/2}q_0^3\frac{\Gamma\left(\kappa-\frac{3}{2}\right)}{\Gamma(\kappa)}. \tag{86}$$

The value of r_0 in (85) ranges between 1 and 10 km according to different sources in the literature. The value of the constant C in (82) is related to the variance $\langle\mu^2\rangle$ of $\mu(\boldsymbol{x})$, which follows immediately the definition (80) and normalization (86):

$$\iiint_{-\infty}^{\infty}\hat{V}(\boldsymbol{q})\,\mathrm{d}\boldsymbol{q} = \langle\mu^2\rangle \quad\Rightarrow\quad C = \frac{\langle\mu^2\rangle\Gamma(\kappa)}{\pi^{\frac{3}{2}}q_0^3\Gamma(\kappa-\frac{3}{2})}. \tag{87}$$

Moreover, because of (84), the correlation function (83) clearly satisfies the necessary and sufficient condition for ergodicity of $\mu(\boldsymbol{x})$ known as the Slutskii theorem (1938), see [44, section 4.7]:

$$\lim_{S\to\infty}\frac{1}{S}\int_0^S V(s)\,\mathrm{d}s = 0.$$

Hence, we can substitute statistical means for spatial averages of μ when averaging over long distances. We also note that in our previous work [3, 6], we have used an approximate value of $\kappa = 2$ instead of $\kappa = \frac{11}{6}$ in formula (82), which simplified the derivation. Moreover, in [38, section 5.1] one can find some experimental data on the spectra of the ionospheric turbulence.

Turbulent fluctuations of the ionosphere will affect the group and phase travel times that are otherwise derived in sections 2 and 3 with no account for randomness. Specifically, in the framework of section 2, we assume that the mean electron number density depends only on the altitude: $\langle n_\mathrm{e}\rangle = \langle n_\mathrm{e}(h)\rangle$. Then, expressions (20) for T_gr and T_ph keep their form, and so do expressions (21) that introduce the average velocities. However, according to (79), instead of formula (24) for the quantity $\bar{\omega}_\mathrm{pe}^2$ that enters into (21), we now need to write

$$\begin{aligned}\bar{\omega}_\mathrm{pe}^2 &= \frac{1}{R_z}\int_0^{R_z}\omega_\mathrm{pe}^2(s)\,\mathrm{d}s = \frac{4\pi e^2}{m_\mathrm{e}R_z}\left[\int_0^H\langle n_\mathrm{e}(h)\rangle\frac{\mathrm{d}h}{\cos\theta}+\int_0^{R_z}\mu(s)\,\mathrm{d}s\right]\\ &= \frac{4\pi e^2}{m_\mathrm{e}H}\int_0^H\langle n_\mathrm{e}(h)\rangle\,\mathrm{d}h+\frac{4\pi e^2}{m_\mathrm{e}R_z}\int_0^{R_z}\mu(s)\,\mathrm{d}s = \frac{4\pi e^2}{m_\mathrm{e}}\frac{N_H}{H}+\frac{4\pi e^2}{m_\mathrm{e}R_z}\int_0^{R_z}\mu(s)\,\mathrm{d}s,\end{aligned} \tag{88}$$

where the new definition of the TEC is (cf formula (25))

$$N_H \stackrel{\text{def}}{=} \int_0^H\langle n_\mathrm{e}(h)\rangle\,\mathrm{d}h. \tag{89}$$

In the case of horizontally inhomogeneous ionosphere (section 3), for the phase travel time T_ph we can write following (51) and taking into account (79),

$$\begin{aligned}T_\mathrm{ph}(\boldsymbol{x},z,\omega) &= \int_0^{R_z}\frac{\mathrm{d}s}{v_\mathrm{ph}(s)}\approx\frac{R_z}{c}-\frac{1}{2c}\int_0^{R_z}\frac{4\pi e^2}{m_\mathrm{e}\omega^2}(\langle n_\mathrm{e}(s)\rangle+\mu(s))\,\mathrm{d}s\\ &= \frac{R_z}{c}-\frac{1}{2c\cos\theta}\int_0^H\frac{4\pi e^2}{m_\mathrm{e}\omega^2}\langle n_\mathrm{e}(\xi_1(h),h)\rangle\,\mathrm{d}h-\frac{1}{2c}\int_0^{R_z}\frac{4\pi e^2}{m_\mathrm{e}\omega^2}\mu(s)\,\mathrm{d}s.\end{aligned} \tag{90}$$

The Taylor formula for $\langle n_e \rangle = \langle n_e(\xi_1, h) \rangle$ yields (cf formula (50))

$$\langle n_e(\xi_1, h) \rangle \approx \langle n_e(0, h) \rangle + \xi_1 \frac{\partial}{\partial \xi_1} \langle n_e(0, h) \rangle, \tag{91}$$

and substituting the right-hand side of (91) into (90), we arrive at the same formula (54) as in section 3, but with the new definitions of some of the expressions that it is comprised of. Namely, the quantity $\bar{\omega}_{pe}^2$ enters into formula (54) through the average velocity $\bar{v}_{ph}(\omega) = c\left(1 + \frac{1}{2}\frac{\bar{\omega}_{pe}^2}{\omega^2}\right)$, see (21), and according to (90), it should now be evaluated as follows (cf formula (88)):

$$\bar{\omega}_{pe}^2 = \frac{4\pi e^2}{m_e}\left[\frac{1}{H}\int_0^H \langle n_e(0, h) \rangle \, dh + \frac{1}{R_z}\int_0^{R_z} \mu(s) \, ds\right] = \frac{4\pi e^2}{m_e}\frac{N_H}{H} + \frac{4\pi e^2}{m_e R_z}\int_0^{R_z} \mu(s) \, ds, \tag{92}$$

so that the TEC is re-defined again, this time via $\langle n_e(0, h) \rangle$ (cf formula (89)):

$$N_H \stackrel{\text{def}}{=} \int_0^H \langle n_e(0, h) \rangle \, dh. \tag{93}$$

Moreover, the first moment $Q(\boldsymbol{x}^0, z)$ that also enters into formula (54) is re-defined in the presence of turbulence according to (91) (cf formula (55)):

$$Q(\boldsymbol{x}^0, z) \stackrel{\text{def}}{=} \frac{1}{H^2}\int_0^H \frac{4\pi e^2}{m_e \bar{\omega}_{pe}^2}\frac{\partial}{\partial \xi_1}\langle n_e(0, h) \rangle h \, dh. \tag{94}$$

In doing so, we emphasize that the factor $\bar{\omega}_{pe}^2$ appears in the second term on the right-hand side of (54) only for the convenience of notation. In fact, this second term does not depend on $\bar{\omega}_{pe}^2$ because this quantity also appears in the denominator in (94). Hence, randomness contributes only to the first term on the right-hand side of (54) via (92).

Along with the travel times, turbulent fluctuations may impact the compression and rate of the propagating pulse. Specifically, formulae (23) and (31) will remain unchanged, but the expression for $\delta\tau$ will now depend on $\bar{\omega}_{pe}^2$ given by (88) or (92). Altogether, the new quantities will affect the dispersive propagator (16), (17), and through it, both the range and azimuthal factors of the GAF, see formulae (28) and (29).

It turns out that the overall effect of turbulent fluctuations on the performance of the SAR sensor in range is small. More precisely, even though the quantity $\bar{\omega}_{pe}^2$ that determines the shape of the propagating pulse (23), (31), as well as the displacement of the target in range (40), contains a stochastic component $\sim \int_0^{R_z} \mu(s) \, ds$, see (88), (92), this component is small because μ is ergodic and $\langle \mu \rangle = 0$. Indeed, let

$$\varphi_0 = \int_0^{R_z} \mu(s) \, ds, \qquad \langle \varphi_0 \rangle = 0, \tag{95}$$

denote the random contribution to the eikonal (up to a constant factor). Then, following [45, chapter I], in the case of a homogeneous plasma we obtain with the help of (87) and (85)

$$\begin{aligned}\langle \varphi_0^2 \rangle &= \pi^2 R_z \int_0^\infty \hat{V}(q) q \, dq = \pi^2 R_z \frac{C q_0^2}{2(\kappa - 1)} \\ &= R_z \langle \mu^2 \rangle \frac{\sqrt{\pi}\Gamma(\kappa)}{2q_0 \Gamma(\kappa - \frac{3}{2})(\kappa - 1)} = \frac{R_z r_0}{2}\langle \mu^2 \rangle.\end{aligned}$$

For the inhomogeneous plasma, we can write following [45, chapter I] and using (81)

$$\begin{aligned}\langle \varphi_0^2 \rangle &\approx \frac{r_0}{2}\int_0^{R_z} \langle \mu^2(s) \rangle \, ds = \frac{r_0}{2} M^2 \int_0^{R_z} \langle n_e(s) \rangle^2 \, ds \\ &= \frac{r_0}{2}\frac{M^2}{\cos\theta}\int_0^H \langle n_e(\xi_1(h), h) \rangle^2 \, dh \stackrel{\text{def}}{=} \frac{r_0}{2}\frac{M^2}{\cos\theta} N_{2,H},\end{aligned} \tag{96}$$

where according to [41], the value of $N_{2,H}$ for high altitudes H is between $9.3 \times 10^{18}\text{cm}^{-5}$ and $9.9 \times 10^{20}\text{cm}^{-5}$, with the average of about $5 \times 10^{19}\text{cm}^{-5}$.

Next, we return to formula (90) for the travel time in the turbulent ionosphere and realize that the second term on its right-hand side accounts for the contribution of the baseline, i.e. deterministic, dispersion, whereas the third term is responsible for that of the turbulent fluctuations. The magnitude of the second term is $\sim \frac{1}{c}\frac{4\pi e^2}{m_e\omega^2}N_H$, while the magnitude of the third, random, term shall be estimated via its standard deviation, which yields $\sim \frac{1}{c}\frac{4\pi e^2}{m_e\omega^2}\sqrt{\langle\varphi_0^2\rangle}$. Hence, the ratio of the third term to the second one is

$$\frac{\sqrt{\langle\varphi_0^2\rangle}}{N_H} \sim \frac{M\sqrt{r_0 N_{2,H}}}{N_H} \ll 1. \tag{97}$$

Indeed, the ratio (97) is approximately between 2×10^{-4} and 7×10^{-4} for the typical parameters listed in table 1, including the correlation length r_0 that ranges between 10^5 cm and 10^6 cm. Similarly, to see what the role of randomness is in determining the shape of the propagating pulse we need to compare the standard deviation $\sqrt{\langle\delta\tau^2\rangle}$ with the mean $\langle\delta\tau\rangle$, where $\delta\tau$ is defined by formula (23) and $\bar{\omega}_{\text{pe}}^2$ is defined by formula (92). It is easy to see that the ratio $\frac{\sqrt{\langle\delta\tau^2\rangle}}{\langle\delta\tau\rangle}$ evaluates to the same quantity as given by formula (97). We therefore conclude that the contribution of turbulent fluctuations to travel times, as well as to the change of the pulse duration and rate in the course of its propagation in the ionosphere, is much smaller than that of the baseline dispersion.

To evaluate the azimuthal factor (29) of the GAF, we denote similar to (95)

$$\varphi_n = \int_0^{R_z} \mu(s)\,\mathrm{d}s, \tag{98}$$

and instead of (42) obtain

$$W_A'(y,z) = \sum_{n=-N/2}^{N/2} \mathrm{e}^{\frac{2i\omega_0}{c}\left(R\Psi_n + \frac{1}{2}\frac{4\pi e^2}{m_e\omega_0^2}\varphi_n\right)}, \tag{99}$$

where (cf formula (56))

$$\Psi_n = -\frac{y_1 x_1^n}{R^2} + \frac{4\pi e^2}{m_e\omega_0^2}\frac{N_H}{H}\frac{\left(x_1^n\right)^2}{4R^2} + \frac{\bar{\omega}_{\text{pe}}^2}{2\omega_0^2}Qx_1. \tag{100}$$

Formula (100) is written under the same assumptions of $z_1 = 0$ and $y_3 = z_3$ as in section 2.2, and the TEC N_H is given by (93). Again, we note that the last term on the right-hand side of (100) does not depend on $\bar{\omega}_{\text{pe}}^2$ because of the definition of Q (94).

Due to the central limit theorem [46, chapter 2], each eikonal φ_n of (98) is a Gaussian random variable with zero mean, $\langle\varphi_n\rangle = 0$. The variances of all individual φ_n can be assumed approximately equal to one another because the variation of the integration distance R_z in (98) with respect to n is small compared to R, see (43):

$$\frac{\omega_0^2}{c^2}\left(\frac{4\pi e^2}{m_e\omega_0^2}\right)^2\langle\varphi_n^2\rangle \approx \sigma^2, \qquad n = -N/2,\ldots,N/2.$$

Then, as shown in [3], we have

$$\langle W_A'(y_1,0)\rangle \;\propto\; \mathrm{e}^{-\sigma^2/2}\sum_{n=-N/2}^{N/2}\mathrm{e}^{\frac{2i\omega_0 R}{c}\Psi_n}, \tag{101}$$

where Ψ_n is given by (100) or, equivalently, (56) in the non-turbulent case. The factor $\mathrm{e}^{-\sigma^2/2}$ in front of the sum on the right-hand side of (101) represents the phenomenon of extinction,

see [45, chapter I]. The value of σ^2 for the typical parameters we have chosen, see table 1, is $\sigma^2 \approx 0.058$ if $r_0 = 1$ km, and $\sigma^2 \approx 0.58$ if $r_0 = 10$ km. Other than the extinction, the sum on the right-hand side of (101) is the same as that in (42); it controls the SAR performance in azimuth in the case of a non-fluctuating ionosphere.

While formula (101) shows that the mean value of the azimuthal factor of the GAF essentially coincides with its deterministic counterpart, the ionospheric turbulence still manifests itself through the presence of random eikonals φ_n in the exponents on the right-hand side of (99). The effect of randomness on the azimuthal resolution is stronger than that on the range resolution. The reason is that the range resolution is basically determined by a single look, and because of the ergodicity the contribution of turbulent fluctuations to the radar reading averages out, see formulae (95)–(97). In contrast, azimuthal resolution is built using multiple looks, $n = -N/2, \ldots, N/2$, and whereas the contribution of randomness to each individual reading is still small, it can get amplified when those readings are summed up.

To quantify this 'un-averaging' effect [3], one needs to estimate the variance of the sum (99). Each term in this sum is a random variable with a logarithmically normal distribution [47], and as long as those variables are uncorrelated, they are also independent [3, appendix F]. Therefore, the covariance of the received signals will also provide a measure of independence for the random variables in the sum (99). If the fluctuations of the phase are small, which is the case for our study, then the correlation function of the field is approximately equal to the correlation function of the electron number density (80), see [45, chapter I]. Therefore, the correlation length r_0 given by formula (85) also provides a characteristic scale of how rapidly the received field decorrelates along the synthetic antenna. Roughly speaking, for the locations that are further apart than r_0, the received pulses will be uncorrelated and hence independent, whereas for the locations that are closer than r_0 they will not be independent.

Therefore, the following expression derived in [3] yields the variance of (99):

$$\sigma_\Sigma^2 \approx \frac{r_0}{L_{\mathrm{SA}}}(N+1)^2\sigma^2, \tag{102}$$

and as also shown in [3], the corresponding relative change of the azimuthal resolution is $\sim \frac{\sigma}{2}\sqrt{\frac{r_0}{L_{\mathrm{SA}}}}$. For the typical parameters (see table 1), this quantity is about 1.7% if $r_0 = 1$ km, and 17% if $r_0 = 10$ km. It may get even higher if the instantaneous values for M and $N_{2,H}$, see (81) and (96), happen to be larger than their typical averages.

The fact that the performance of the SAR system in range is only weakly sensitive to turbulent fluctuations indicates that the ionospheric turbulence will basically not affect any of the considerations of sections 4 and 5 related to reconstructing the TEC with the help of formula (59), improving the robustness of reconstruction by means of the image registration, and assessing the quality of the image obtained with the corrected filter. At the same time, as the random contribution to individual travel times averages out, the proposed filter correction is essentially based on deterministic quantities only. As such, we do not expect that it will provide an efficient means for reducing the ionospheric distortions of the image that are due to the turbulence.

It is also to be noted that the conditioning of formula (60) may be better than that of formula (59) because the individual quantities $y_1^{(1)}$ and $y_1^{(2)}$ may not be as large compared to the azimuthal shift Δy_1. There may, however, be a potential difficulty of a different nature in evaluating Q by formula (60), because unlike the range resolution, the azimuthal resolution of a SAR system is sensitive to the turbulent fluctuations of the ionosphere, see formula (102). This sensitivity may induce larger errors in $y_1^{(1)}$ and $y_1^{(2)}$. Addressing the accuracy considerations for Q will be a subject of future study.

7. Discussion

In our previous work, we introduced the dual carrier probing as a means of reconstructing the ionospheric TEC when imaging the Earth's surface by a spaceborne SAR. The value of the reconstructed TEC is subsequently used to correct the matched filter, which is a key component of the SAR signal processing algorithm, and thus reduce or remove the ionospheric distortions that would otherwise appear on the image.

In this paper, we have proposed to use the area-based image registration for improving the accuracy and robustness of the reconstructed TEC. In particular, we have related the error of the registration to that of the TEC reconstruction, and have also shown how the error of the TEC affects the final quality of the re-processed image. Although the interferometric methods of [11, 14] may be more accurate, the proposed methodology still leads to a multi-fold reduction of the image artifacts caused by the ionosphere in their part which is not due to the turbulence. An important advantage of the proposed methodology though is that it requires neither the ground-based receivers (like GPS does) nor a repeat satellite pass.

Additional contributions of the current paper include a more accurate account of the effect of turbulent fluctuations on the image based on the true Kolmogorov–Obukhov spectrum of turbulence, as well as an account of Ohmic losses in the ionospheric plasma and an account of the horizontal inhomogeneity of the ionosphere. In regard to the latter, we note that whereas our description predicts that the sign of the azimuthal displacement S_A and that of the first moment Q will be the same, see formula (57), other descriptions in the literature may have those signs as opposite, see, e.g., [48–50]. We attribute this discrepancy to the difference in the definition of S_A.

The issues that may require further attention include the following.

- *Studying the possibility of iterative application of registration/correction procedures*. Even if the first correction is not perfect (say, because the images are blurry and cannot be matched well enough), the improvement of the image quality may result in better registration of the two corrected images.
- *Analysis of SAR imaging through the ionosphere with the polarization of the interrogating field taken into account*. It should include the anisotropy of the plasma due to the magnetic field of the Earth (gyrotropy), and may also touch upon the possible anisotropy at the target, as in [51]. Our preliminary considerations suggest that the effect of the magnetic field of the Earth on the dispersion of radio waves in the ionosphere is negligible. Hence, the two key components—dispersive propagation and the Faraday rotation—decouple and can be studied independently. Regarding the Faraday rotation, an important objective is to see whether the dual carrier probing can help reduce or remove its potential detrimental effect on the image in the case where the SAR instrument does not have a fully polarimetric capability.
- *Analysis of the linearized scattering off dispersive targets*. Dispersion of the target material is a key characteristic that may enable its identification [52]. The goal is to build a mathematical model for SAR imaging that includes the dispersion of the target, with possible future applications to miSAR, and with the potential of distinguishing between the target dispersion and the ionospheric dispersion.
- *A more thorough analysis of the stochastic component of ionospheric distortions using the turbulence structure function* [45] *rather than the correlation function*. Analysis of the effect of turbulent fluctuations of the electron number density in the ionosphere on the SAR image in the case where the statistics of waves (mainly, that of the eikonal) does not necessarily coincide with the statistics of the medium. Study of the anisotropic turbulence due to the magnetic field of the Earth. Development of appropriate strategies of how to

additionally correct the matched filter in order to reduce the stochastic part of ionospheric distortions, assuming that the statistics of waves is known.

- Given that the current mitigation strategy based on dual carrier probing is effective mostly for the deterministic part of ionospheric distortions, an investigation may be warranted of whether the stochastic component of distortions can be tackled by any of the general 'black box' image sharpening and deblurring techniques [53] developed previously with no direct relation to spaceborne SAR.
- Analysis of the linearized scattering of the polarized radio waves off rough surfaces, with the goal of relating SAR imaging to a physical mechanism of backscattering at the target.
- An in-depth investigation of the VHF SAR imaging through the ionosphere aimed at determining whether the VHF frequencies (very low in the SAR context yet still above the Langmuir frequency) may require a more comprehensive propagation model that would include, for example, kinetic considerations [2].

Acknowledgments

This work was supported by the US Air Force Office of Scientific Research (AFOSR) under agreement FA9550-10-1-0092. We would also like to thank the anonymous referees of our paper for their helpful comments.

Appendix A. Propagation of SAR signals in a lossless homogeneous plasma

In this section, we re-derive the results of [6, appendix A] in a more concise yet consistent way. We are interested in obtaining a spherically symmetric solution similar to the retarded potential (7), but for the case of a dispersive propagation governed by the Klein–Gordon equation (1) with $\omega_{\rm pe} = \text{const}$. Let $r = |z - \boldsymbol{x}|$ denote the radial coordinate in the spherical system centered at $\boldsymbol{x} \in \mathbb{R}^3$, which is the location of the antenna (we are using the notations of section 2.1), and let $\varphi = \varphi(t, r)$ be a spherically symmetric solution of equation (1). Introduce a new function $\phi = \phi(t, r)$, such that $\varphi(t, r) = \phi(t, r)/r$. Then, $\phi(t, r)$ satisfies the one-dimensional Klein–Gordon equation:

$$\frac{\partial^2 \phi}{\partial t^2} - c^2 \frac{\partial^2 \phi}{\partial r^2} + \omega_{\rm pe}^2 \phi = 0, \qquad r \geqslant 0. \tag{A.1}$$

Hence, we need to look into the propagation of pulses governed by equation (A.1).

Assume that a pulse of shape $P(t)$ is given at $r = 0$ (location of the antenna); for example, it can be the high-range resolution upchirp (6):

$$P(t) = \frac{1}{4\pi} \chi_\tau(t)\, \mathrm{e}^{\mathrm{i}(\omega_0 + \frac{Bt}{2\tau})t}, \tag{A.2}$$

where ω_0 is the center carrier frequency, B is the angular bandwidth and τ is the duration of the chirp. The factor $1/4\pi$ in (A.2) accounts for the difference between the one-dimensional and three-dimensional delta-functions $\delta(r)$ and $\delta(x_1, x_2, x_3)$ that excite the pulse at the origin.

A Fourier transform in time of the pulse (A.2) is expressed via the erf functions. The latter can subsequently be evaluated with the help of the stationary phase method, see [6, appendix A]. If, in doing so, the transient behavior near the endpoints of the pulse frequency range is disregarded, i.e. if we leave out the cases $|\omega_0 - B/2 - \omega| \ll B$ and $|\omega_0 + B/2 - \omega| \ll B$, then the resulting transform $\hat{P}(\omega)$ approximately represents the chirp at $t = 0$ as a superposition of sinusoidal harmonics with different frequencies:

$$\hat{P}(\omega) \approx \begin{cases} -\dfrac{1}{8\pi^2} \dfrac{\sqrt{\pi}}{\sqrt{\alpha}} \mathrm{e}^{-\mathrm{i}\frac{\beta^2}{4\alpha} + \mathrm{i}\frac{\pi}{4}}, & \text{if } \omega \in [\omega_0 - B/2, \omega_0 + B/2], \\ 0, & \text{if } \omega \notin [\omega_0 - B/2, \omega_0 + B/2]. \end{cases} \tag{A.3}$$

where $\beta = \omega - \omega_0$. Each of the frequencies ω that compose the spectrum in (A.3), or, rather, each of the harmonics $e^{i\omega t}$, propagates with its own phase velocity of (5). Indeed, the propagating pulse $\phi(t, r)$ that has covered the distance r from the origin can be written as the inverse Fourier transform [54, chapter I], which, according to (2), immediately leads to the introduction of the phase velocity $v_{ph} = \omega/k$ in the exponent:

$$\phi(t, z) = \int_{\omega_0 - B/2}^{\omega_0 + B/2} \hat{P}(\omega)\, e^{i(\omega t - kr)}\, d\omega = \int_{\omega_0 - B/2}^{\omega_0 + B/2} \hat{P}(\omega)\, e^{i\omega(t - r/v_{ph})}\, d\omega. \tag{A.4}$$

In (A.4), the phase velocity v_{ph} and wavenumber k are assumed to be the functions of the frequency ω defined by the dispersion relation (3). Introducing

$$\frac{1}{v_{ph_0}} = \left.\frac{k}{\omega}\right|_{\omega_0} \quad \text{and} \quad \frac{1}{v_{gr_0}} = \left.\frac{dk}{d\omega}\right|_{\omega_0} \tag{A.5}$$

and using (3) and (5), we can approximately represent $(\omega t - kr)$ in (A.4) by means of the Taylor formula:

$$\begin{aligned}\omega t - kr = \omega\left(t - \frac{r}{v_{ph}(\omega)}\right) &\approx (\omega_0 + \beta)\left[t - r\left(\frac{1}{v_{ph}} + \beta\frac{d}{d\omega}\frac{1}{v_{ph}} + \frac{\beta^2}{2}\frac{d^2}{d\omega^2}\frac{1}{v_{ph}}\right)\Bigg|_{\omega_0}\right] \\ &= \omega_0\left(t - \frac{r}{v_{ph_0}}\right) + b\beta - rb_2\beta^2,\end{aligned} \tag{A.6}$$

where

$$\begin{aligned} b &= t - \frac{r}{v_{ph_0}} - \omega_0 r \left.\frac{d}{d\omega}\frac{1}{v_{ph}}\right|_{\omega_0} = t - \frac{r}{v_{gr_0}}, \\ b_2 &= \left.\frac{d}{d\omega}\frac{1}{v_{ph}}\right|_{\omega_0} + \frac{\omega_0}{2}\left.\frac{d^2}{d\omega^2}\frac{1}{v_{ph}}\right|_{\omega_0} \approx -\frac{1}{2c}\frac{\omega_{pe}^2}{\omega_0^3}. \end{aligned} \tag{A.7}$$

Substituting (A.6) and (A.7) into (A.4) and changing the integral over ω to that over β, we obtain

$$\begin{aligned}\phi(t, z) &= -\frac{1}{8\pi^2}\frac{\sqrt{\pi}}{\sqrt{\alpha}} e^{i\frac{\pi}{4}} \int_{-B/2}^{B/2} e^{-i\frac{\tau}{2B}\beta^2} e^{i\omega_0(t - r/v_{ph_0})} e^{ib\beta - irb_2\beta^2}\, d\beta \\ &= -\frac{1}{8\pi^2}\frac{\sqrt{\pi}}{\sqrt{\alpha}} e^{i\frac{\pi}{4}} e^{i\omega_0(t - r/v_{ph_0})} \int_{-B/2}^{B/2} e^{-ia\beta^2 + ib\beta}\, d\beta \\ &= -\frac{1}{8\pi^2}\frac{\sqrt{\pi}}{\sqrt{\alpha}} e^{i\frac{\pi}{4}} \frac{\sqrt{\pi}}{2\sqrt{a}} e^{i\frac{b^2}{4a}} e^{-i\frac{\pi}{4}} e^{i\omega_0(t - r/v_{ph_0})} \left[\operatorname{erf}\left(\frac{\sqrt{i}(b + aB)}{2\sqrt{a}}\right) - \operatorname{erf}\left(\frac{\sqrt{i}(b - aB)}{2\sqrt{a}}\right)\right] \\ &= \frac{1}{16\pi\sqrt{\alpha}\sqrt{a}} e^{i\omega_0(t - r/v_{ph_0})} e^{i\frac{b^2}{4a}} \left[\operatorname{erf}\left(\frac{\sqrt{i}(b - aB)}{2\sqrt{a}}\right) - \operatorname{erf}\left(\frac{\sqrt{i}(b + aB)}{2\sqrt{a}}\right)\right], \end{aligned} \tag{A.8}$$

where

$$a = \frac{\tau}{2B} + rb_2 \equiv \frac{\tau}{2B} - \frac{1}{2}\frac{r}{c}\frac{\omega_{pe}^2}{\omega_0^3} \tag{A.9}$$

and the branch of the square root is chosen such that $|\arg(\cdot)| \leqslant \pi$.

Using a stationary phase argument one more time, we have shown in [6, appendix A] that the difference of the two erf functions in the last line of (A.8) is equal to 2 if the value of b is within the interval of $(-aB, aB)$, and zero otherwise[9]. Introducing

$$\eta_\pm = \frac{b \pm aB}{2\sqrt{a}}, \tag{A.10}$$

[9] Although the integral in the second line of (A.8) is algebraically of the same type as that in (33), the analysis of section 2.2 does not apply here because the QPE for (A.8) is not small: $\phi_{qB} \approx B\tau/8 \gg 1$.

we can rewrite this difference as follows:

$$[\operatorname{erf}(\sqrt{\mathrm{i}}\eta_-) - \operatorname{erf}(\sqrt{\mathrm{i}}\eta_+)] = 2\chi_{\tau'}(b), \tag{A.11}$$

where χ is the indicator function defined in (6), and

$$\tau' \stackrel{\text{def}}{=} 2aB = \tau - \frac{r}{c}\frac{\omega_{\text{pe}}^2}{\omega_0^2}\frac{B}{\omega_0} = \tau - \delta\tau \tag{A.12}$$

is a new pulse length. Accordingly, the quantity

$$\alpha' \stackrel{\text{def}}{=} \frac{1}{4a} = \frac{B}{2\tau'} \approx \frac{B}{2\tau}\left(1 + \frac{\delta\tau}{\tau}\right) = \alpha + \delta\alpha \tag{A.13}$$

becomes a new chirp rate (see the second exponent in the last line of (A.8)).

Altogether, combining formulae (A.8)–(A.13), using the notation of (6) and recalling that $\varphi(t, r) = \phi(t, r)/r$, we obtain the spherically symmetric propagating pulse in the form

$$\begin{aligned}\varphi(t, r) &= \frac{1}{4\pi r}\mathrm{e}^{\mathrm{i}\omega_0(t - r/v_{\text{ph}_0})}\chi_{\tau'}(t - r/v_{\text{gr}_0})\,\mathrm{e}^{\mathrm{i}\alpha'(t - r/v_{\text{gr}_0})^2} \\ &\stackrel{\text{def}}{=} \frac{1}{4\pi r}A'(t - r/v_{\text{gr}_0})\,\mathrm{e}^{\mathrm{i}\omega_0(t - r/v_{\text{ph}_0})}.\end{aligned} \tag{A.14}$$

Remark. Leaving out the transients that correspond to the endpoints of the pulse and its spectrum when using the stationary pause method is equivalent to disregarding the so-called precursors, see [2, section 21] or [55]. In other words, we are focusing on the propagation of the main body of the pulse because it is the main body of the pulse that is used for building the generalized ambiguity function in section 2.

Remark. The observation that $\tau' < \tau$ (and, consequently, $\alpha' > \alpha$) for an upchirp ($\alpha > 0$, see (6)) agrees with the formula for the group velocity in (5). Indeed, for an upchirp the slower propagating low-frequency harmonics are emitted first and the faster propagating high-frequency harmonics are emitted last. Hence, the 'tail' of the chirp travels faster than its 'head,' which results in the pulse compression. The situation for the downchirp ($\alpha < 0$) will be the opposite: it will get dilated rather than compressed, $\tau' > \tau$, while its absolute rate will become lower rather than higher, $|\alpha'| < |\alpha|$ (see also [24, figure 1]).

Remark. Using expressions (A.4) and (14), one can represent the range factor of the GAF as a double integral in frequency ω and fast time t. In [56], the authors adopt this approach and consider Gaussian pulses, which allows them to express the integrals over t and ω in elementary functions. For the rectangular chirp (6), this method would still yield the erf functions at the first step (integration over t), and will thus have no advantage over the one used in the current work.

Appendix B. Propagation of SAR signals in a plasma with losses

Ohmic losses in the ionosphere are due to the collisions of particles. Let $\gamma > 0$ denote the effective collision frequency [2]. Then, the dielectric constant of the ionospheric plasma is given by the following expression (cf formula (4)):

$$\frac{k^2c^2}{\omega^2} = \varepsilon' = 1 - \frac{\omega_{\text{pe}}^2}{\omega(\omega - \mathrm{i}\gamma)}. \tag{B.1}$$

The value of γ in the ionosphere depends on the altitude, solar activity and the time of the day, but generally it does not exceed 10^5 Hz [57, 2], i.e. $\gamma \ll \omega$. Under this condition, the solution $k^* = k^*(\omega)$ to equation (B.1) will have a small imaginary part[10]:

$$k^* = \frac{\omega}{c}\left(1 - \frac{1}{2}\frac{\omega_{\rm pe}^2}{\omega^2} - \frac{\mathrm{i}}{2}\frac{\omega_{\rm pe}^2}{\omega^2}\frac{\gamma}{\omega}\right).$$

Similarly, the expressions in (A.5), (A.7) and (A.9) will all acquire small imaginary parts proportional to γ:

$$\begin{aligned}
&\frac{1}{v_{{\rm ph}_0}^*} = \frac{1}{v_{{\rm ph}_0}} - \frac{\mathrm{i}}{2}\frac{1}{c}\frac{\gamma\omega_{\rm pe}^2}{\omega_0^3},\\
&b^* = b - \mathrm{i}\frac{r}{c}\frac{\gamma\omega_{\rm pe}^2}{2\omega_0^3},\\
&b_2^* = b_2 - \mathrm{i}\frac{3}{2}\frac{\gamma\omega_{\rm pe}^2}{c\omega_0^4},\\
&a^* = \frac{\tau}{2B} + rb_2^* = a - \mathrm{i}\frac{3}{2}\frac{\gamma r}{c}\frac{\omega_{\rm pe}^2}{\omega_0^4}.
\end{aligned} \tag{B.2}$$

The reasoning in appendix A that leads to formula (A.8) will hold in the lossy case with the replacement of the variables $(a, b, b_2, v_{{\rm ph}_0})$ by $(a^*, b^*, b_2^*, v_{{\rm ph}_0}^*)$ given by (B.2). The overall effect of complexity in (B.2) is as follows. First, it causes a gradual exponential attenuation of the propagating wave:

$$\mathrm{e}^{\mathrm{i}\omega_0(t-r/v_{{\rm ph}_0}^*)} = \mathrm{e}^{\mathrm{i}\omega_0(t-r/v_{{\rm ph}_0})}\mathrm{e}^{-\frac{1}{2}\frac{r}{c}\frac{\gamma\omega_{\rm pe}^2}{\omega_0^2}}. \tag{B.3}$$

Other than that, we can write

$$\mathrm{e}^{\mathrm{i}\frac{(b^*)^2}{4a^*}} = \mathrm{e}^{\mathrm{i}\frac{b^2}{4a}}\mathrm{e}^{\mathrm{i}\left(\frac{(b^*)^2}{4a^*} - \frac{b^2}{4a}\right)} = \mathrm{e}^{\mathrm{i}\frac{b^2}{4a}}\mathrm{e}^{\mathrm{i}\left(-\frac{2\mathrm{i}b}{4a}\frac{r}{c}\frac{\gamma\omega_{\rm pe}^2}{2\omega_0^3}\right)} = \mathrm{e}^{\mathrm{i}\frac{b^2}{4a}}\mathrm{e}^{\frac{b}{2a}\frac{r}{c}\frac{\gamma\omega_{\rm pe}^2}{2\omega_0^3}},$$

and using (A.11), (A.12): $|b| \leqslant \tau'/2 = aB$, conclude that the second exponent in the previous equality satisfies

$$\left|\frac{b}{2a}\frac{r}{c}\frac{\gamma\omega_{\rm pe}^2}{2\omega_0^3}\right| \leqslant \frac{1}{4}\frac{r}{c}\frac{\gamma\omega_{\rm pe}^2}{\omega_0^2}\frac{B}{\omega_0}.$$

The corresponding exponential function may be either decreasing or increasing, but either way the rate of its amplitude change will be much slower than that in (B.3) because of an additional small factor $\frac{B}{\omega_0} \ll 1$ in the exponent.

Using (A.10), we can also introduce $\eta_\pm^*$ by substituting the corresponding complex quantities from (B.2), and define $\delta\eta_\pm \stackrel{\rm def}{=} \eta_\pm^* - \eta_\pm$, where

$$|\delta\eta_\pm| \sim \frac{1}{2}\sqrt{\frac{2B}{\tau}}\frac{r}{c}\frac{\gamma\omega_{\rm pe}^2}{2\omega^3} \ll 1.$$

Then, for the difference between the erf functions of the complex argument $\eta_\pm^*$ and the real argument $\eta_\pm$, we have

$$\left|\mathrm{erf}(\sqrt{\mathrm{i}}(\eta_\pm + \delta\eta_\pm)) - \mathrm{erf}(\sqrt{\mathrm{i}}\eta_\pm)\right| \approx \left|\frac{2}{\sqrt{\pi}}\mathrm{e}^{-\mathrm{i}\eta_\pm^2}\cdot\sqrt{\mathrm{i}}\delta\eta_\pm\right| = \frac{2}{\sqrt{\pi}}|\delta\eta_\pm|.$$

[10] In this appendix, the asterisk superscript will denote the quantities that pertain to the lossy case.

Consequently, the total variation of the quantity $[\mathrm{erf}(\sqrt{\mathrm{i}}\eta_-^*) - \mathrm{erf}(\sqrt{\mathrm{i}}\eta_+^*)]$ that appears in the 'lossy' counterpart of (A.8) will not exceed $\frac{4}{\sqrt{\pi}}|\delta\eta_\pm|$ by absolute value, which is a negligible contribution compared to the value of 2 in the lossless case.

Altogether, using (B.3) and disregarding other effects of complexity, we obtain the following form of the propagating signal in the case of a lossy plasma (cf formula (A.14)):

$$\varphi(t,r) \approx \frac{1}{4\pi r} A'(t - r/v_{\mathrm{gr}_0}) \mathrm{e}^{\mathrm{i}\omega_0(t-r/v_{\mathrm{ph}_0})} \mathrm{e}^{-\frac{1}{2}\frac{r}{c}\frac{\gamma\omega_{\mathrm{pe}}^2}{\omega_0^2}}. \tag{B.4}$$

Appendix C. Area-based image registration for dual carrier probing

In this appendix, we show how one can reduce the error of the area-based image registration due to the discrete Fourier transform and due to noise. Possible misregistration due to different terrain reflectivity on two different carrier frequencies belongs to neither of these two categories and is not discussed hereafter. Note also that while we are proposing to use the area-based image registration for correcting the matched filter in SAR signal processing, it is otherwise used routinely for SAR interferometry, see, e.g. [40]. Our subsequent discussion focuses on one-dimensional signals for simplicity; the extension to two dimensions can be found, e.g., in [26, 27].

The phase correlation method is based on formula (61), which is written for two continuous one-dimensional signals $u(x)$ and $v(x)$ defined on $-\infty < x < \infty$. In practice, however, the signals are discrete rather than continuous, and their length is finite. Let us therefore introduce two sequences of length L: $\{u_l\}_{l=0}^{L-1}$ and $\{v_l\}_{l=0}^{L-1}$, and interpret them as traces of two continuous functions, $u(x)$ and $v(x) = u(x-s)$, on a uniform grid of size T:[11] $u_l \equiv u(x_l)$ and $v_l \equiv v(x_l)$, where $x_l = lT$ and $l = 0, 1, \ldots, L-1$. Clearly, the lower bound for T is the pixel size, whereas the upper bound for L is the total number of pixels in those fragments of each image that are employed for registration. Instead of (61), we will use the discrete Fourier transform (see, e.g., [58, section 5.7]) of u_l and v_l (which assumes, in particular, that both sequences are L-periodic):

$$\hat{u}_k = \frac{1}{\sqrt{L}} \sum_{l=0}^{L-1} u_l \, \mathrm{e}^{-\mathrm{i}k\frac{2\pi}{LT}x_l} = \frac{1}{\sqrt{L}} \sum_{l=0}^{L-1} u_l \, \mathrm{e}^{-\mathrm{i}k\frac{2\pi}{L}l} \tag{C.1a}$$

and

$$\begin{aligned} \hat{v}_k &= \frac{1}{\sqrt{L}} \sum_{l=0}^{L-1} v_l \, \mathrm{e}^{-\mathrm{i}k\frac{2\pi}{LT}x_l} = \frac{1}{\sqrt{L}} \sum_{l=0}^{L-1} u(x_l - s) \, \mathrm{e}^{-\mathrm{i}k\frac{2\pi}{LT}x_l} \\ &= \frac{1}{\sqrt{L}} \sum_{l=0}^{L-1} u(x_l - s) \, \mathrm{e}^{-\mathrm{i}k\frac{2\pi}{LT}(x_l - s)} \cdot \mathrm{e}^{-\mathrm{i}k\frac{2\pi}{LT}s} \approx \hat{u}_k \, \mathrm{e}^{-\mathrm{i}k\frac{2\pi}{LT}s}. \end{aligned} \tag{C.1b}$$

Note that the last equality of (C.1*b*) is only approximate rather than exact because of the error that may appear if the shift s is not a multiple of the grid size T. For smooth periodic functions though, this error can be shown to decay rapidly as L increases (see, e.g., the analysis in [58, sections 3.1 and 4.1]), and we therefore disregard it hereafter.

Next, we build a discrete function similar to that of (62):

$$\tilde{\delta}_l \stackrel{\mathrm{def}}{=} \frac{1}{\sqrt{L}} \sum_{k=0}^{L-1} \frac{\hat{u}_k^* \hat{v}_k}{|\hat{u}_k^* \hat{v}_k|} \mathrm{e}^{\mathrm{i}k\frac{2\pi}{LT}x_l} = \frac{1}{\sqrt{L}} \sum_{k=0}^{L-1} \mathrm{e}^{-\mathrm{i}k\frac{2\pi}{LT}s} \mathrm{e}^{\mathrm{i}k\frac{2\pi}{LT}x_l} = \frac{1}{\sqrt{L}} \sum_{k=0}^{L-1} \mathrm{e}^{\mathrm{i}k\frac{2\pi}{L}\left(l - \frac{s}{T}\right)}. \tag{C.2}$$

[11] In the image registration literature, the grid size T is often called the sampling rate, and accordingly, the grid dimension (length of sequence) L is referred to as the number of samples, see, e.g., [39].

To analyze $\tilde{\delta}_l$ of (C.2), we consider two cases: $\frac{s}{T}$ is an integer and $\frac{s}{T}$ is not an integer. First, let $\frac{s}{T} = m \in \mathbb{N}$. Then, from (C.2) we can derive

$$\tilde{\delta}_l = \frac{1}{\sqrt{L}} \sum_{k=0}^{L-1} \mathrm{e}^{\mathrm{i}k\frac{2\pi}{L}(l-m)} = \begin{cases} \sqrt{L}, & \text{if } l = m, \\ \dfrac{1}{\sqrt{L}} \dfrac{1-\mathrm{e}^{\mathrm{i}2\pi(l-m)}}{1-\mathrm{e}^{\mathrm{i}\frac{2\pi}{L}(l-m)}} = 0, & \text{if } l \neq m. \end{cases}$$

In other words, if the shift s happens to be a shift by the integer number m of grid cells, then the function $\tilde{\delta}_l$ of (C.2) has a peak value of $\sqrt{L}$ precisely at $l = m$, and is equal to zero everywhere else on the grid. Hence, in this case the discrete version of phase correlation will yield the value of the shift exactly.

If $\frac{s}{T}$ is not an integer, then using (C.2) and assuming that l is close to $\frac{s}{T}$ we obtain

$$\begin{aligned} \tilde{\delta}_l &= \frac{1}{\sqrt{L}} \frac{1-\mathrm{e}^{\mathrm{i}2\pi\left(l-\frac{s}{T}\right)}}{1-\mathrm{e}^{\mathrm{i}\frac{2\pi}{L}\left(l-\frac{s}{T}\right)}} \\ &\approx \frac{\sqrt{L}}{2} \mathrm{e}^{\mathrm{i}\pi\left(l-\frac{s}{T}\right)} \frac{\mathrm{e}^{-\mathrm{i}\pi\left(l-\frac{s}{T}\right)} - \mathrm{e}^{\mathrm{i}\pi\left(l-\frac{s}{T}\right)}}{-\mathrm{i}\pi\left(l-\frac{s}{T}\right)} = \sqrt{L}\,\mathrm{e}^{\mathrm{i}\pi\left(l-\frac{s}{T}\right)} \frac{\sin\pi\left(l-\frac{s}{T}\right)}{\pi\left(l-\frac{s}{T}\right)}, \end{aligned}$$

which means that the maximum absolute value of $\tilde{\delta}_l$ is $\sim \sqrt{L}$, and it is attained at the grid node l closest to $\frac{s}{T}$. At all other grid nodes, generally speaking, $\tilde{\delta}_l \neq 0$. Therefore, if $\frac{s}{T}$ is not an integer, the best accuracy of reconstructing the shift s that one can achieve by looking for the maximum of $\tilde{\delta}_l$ of (C.2) is roughly $T/2$, i.e. at most half size of the pixel. Extension of this method to the accuracies on the order of a fraction of one pixel may involve a certain interpolation procedure, see, e.g., [30], and also [39, 28]. The effects of aliasing and aperiodicity can be reduced by filtering, see [26, 27].

Another approach to further improving the accuracy of phase correlation is based on analyzing the phase of $\hat{u}_k$ and $\hat{v}_k$ of (C.1). Namely, it is easy to see from (C.1*b*) that

$$\arg\hat{u}_k - \arg\hat{v}_k = k\frac{2\pi}{LT}s. \tag{C.3}$$

Speaking formally, the value of s can be obtained from (C.3) by merely dividing the left-hand side of the equality by $k\frac{2\pi}{LT}$ for any non-zero k:

$$s = \frac{LT}{2\pi} \frac{\arg\hat{u}_k - \arg\hat{v}_k}{k}. \tag{C.4}$$

This formula, however, is prone to inaccuracies due to errors in the data $\arg\hat{u}_k - \arg\hat{v}_k$. The way to improve the accuracy is to obtain s by the method of least-squares using all ks rather than only one as in (C.4), see [27, 39]. Namely, s shall be sought for as a solution to the following quadratic minimization problem (see, e.g., [58, chapter 7]):

$$\min_s \sum_{k=1}^{L-1} \left[k\frac{2\pi}{LT}s - (\arg\hat{u}_k - \arg\hat{v}_k) \right]^2. \tag{C.5}$$

The stationary point of the functional in (C.5) can be found by requiring that its first derivative with respect to s be equal to zero, which yields

$$s = \frac{LT}{2\pi} \frac{\sum_{k=1}^{L-1} k(\arg\hat{u}_k - \arg\hat{v}_k)}{\sum_{k=1}^{L-1} k^2}. \tag{C.6}$$

Let us now interpret the data $\{\arg\hat{u}_k - \arg\hat{v}_k\}$, $k = 1, 2, \ldots, L-1$, as independent identically distributed random variables[12] with variances

$$\mathrm{Var}(\arg\hat{u}_k - \arg\hat{v}_k) \stackrel{\mathrm{def}}{=} \langle (\arg\hat{u}_k - \arg\hat{v}_k - \langle \arg\hat{u}_k - \arg\hat{v}_k \rangle)^2 \rangle = \sigma^2.$$

[12] The requirement of independence is important. However, the requirement that all random variables be identically distributed can be alleviated.

The actual errors in the data may be due to the terrain noise, as well as measurement errors, instrument noise, etc. In all those cases, it is convenient to use the description in the form of random variables. Then, $\mathrm{Var}(k(\arg\hat{u}_k - \arg\hat{v}_k)) = k^2\sigma^2$, and according to (C.6) we can write (see, e.g., [46, chapter 2])

$$\begin{aligned}\mathrm{Var}(s) &= \left(\frac{LT}{2\pi}\right)^2 \frac{\sum_{k=1}^{L-1} k^2\sigma^2}{\left(\sum_{k=1}^{L-1} k^2\right)^2} \\ &= \left(\frac{LT}{2\pi}\right)^2 \frac{\sigma^2}{\sum_{k=1}^{L-1} k^2} = \left(\frac{LT}{2\pi}\right)^2 \frac{6\sigma^2}{(L-1)L(2L-1)}.\end{aligned} \tag{C.7}$$

From formula (C.7), one can easily deduce that for sufficiently large L the standard deviation of the shift s determined by the least-squares fit according to (C.6) is

$$\sigma(s) = \sqrt{\mathrm{Var}(s)} \sim \frac{\sigma}{\sqrt{L}}. \tag{C.8}$$

In other words, the error of obtaining the shift by phase correlation scales as the inverse square root of the number of samples L. While formula (C.8) describes the asymptotic behavior of the error, the practical values of the registration accuracy can be as low as only a few per cent of a pixel, see [26–30], i.e. a few per cent of the resolution cell.

Appendix D. Split bandwidth setup for dual carrier probing

Linear chirps of section 2.1 represent a natural waveform for the split bandwidth approach. Indeed, partitioning such a chirp in time causes a proportional partition in frequency, and the other way around. For example, the chirp (6) given by $P(t) = \mathrm{e}^{\mathrm{i}\alpha t^2}\mathrm{e}^{\mathrm{i}\omega_0 t}$ on the interval $[-\tau/2, \tau/2]$ with the rate $\alpha = \frac{B}{2\tau}$ and angular bandwidth B centered around ω_0 can be considered as a combination of two successive sub-chirps:

$$P^{(1)}(t) = \mathrm{e}^{\mathrm{i}\alpha t^2}\mathrm{e}^{\mathrm{i}\omega_0 t} \quad \text{for } t \in [-\tau/2, 0] \quad \text{and} \quad P^{(2)}(t) = \mathrm{e}^{\mathrm{i}\alpha t^2}\mathrm{e}^{\mathrm{i}\omega_0 t} \quad \text{for } t \in [0, \tau/2].$$

Obviously, the frequency intervals for sub-chirps $P^{(1)}(t)$ and $P^{(2)}(t)$ are $[\omega_0 - B/2, \omega_0]$ and $[\omega_0, \omega_0 + B/2]$, respectively. Next, consider a new half-length envelope:

$$A_{\tau/2}(t) \stackrel{\text{def}}{=} \chi_{\tau/2}(t)\,\mathrm{e}^{\mathrm{i}\alpha t^2}, \quad \text{where} \quad \chi_{\tau/2}(t) = \begin{cases} 1, & t \in [-\tau/4, \tau/4], \\ 0, & \text{otherwise.} \end{cases}$$

Then, it is easy to show that

$$\begin{aligned} P^{(1)}(t) &= \mathrm{e}^{\mathrm{i}\alpha\frac{\tau^2}{16} - \mathrm{i}\omega_0\frac{\tau}{4}} P_1(t + \tau/4), \\ P^{(2)}(t) &= \mathrm{e}^{\mathrm{i}\alpha\frac{\tau^2}{16} + \mathrm{i}\omega_0\frac{\tau}{4}} P_2(t - \tau/4), \end{aligned} \tag{D.1}$$

where

$$P_{1,2}(t) \stackrel{\text{def}}{=} A_{\tau/2}(t)\,\mathrm{e}^{\mathrm{i}\omega_{1,2}t}, \quad \omega_{1,2} = \omega_0 \mp \frac{B}{4} \quad \text{and} \quad t \in [-\tau/4, \tau/4]. \tag{D.2}$$

In other words, up to a constant factor of magnitude 1, the sub-chirps $P^{(1)}(t)$ and $P^{(2)}(t)$ are equivalent to time-shifted half-length half-bandwidth linear chirps P_1 and P_2 of (D.2) that are centered around ω_1 and ω_2, respectively, and have the same rate $\alpha = \frac{B}{2\tau}$. Consequently, by processing the same raw data first by means of the filter $\overline{P_1(t + \tau/4 - |\boldsymbol{x} - \boldsymbol{y}|/c)}$ and then by means of $\overline{P_2(t - \tau/4 - |\boldsymbol{x} - \boldsymbol{y}|/c)}$, we will obtain two images on two frequencies ω_1 and ω_2. Due to the ionosphere, these images will be shifted with respect to one another. Hence, they can be used for reconstructing the TEC N_H and its first moment Q according to the methodology of section 4.

Of course, it is also possible to define sub-chirps with the sub-bandwidth b taking any value in the interval $(0, B)$ other than $b = B/2$. The expression for sub-chirp central frequencies is then $\omega_{1,2} = \omega_0 \mp (B - b)/2$. If $b < B/2$, then the central part of the received signal and the central frequencies of the main chirp bandwidth will not be used for any of the sub-images, whereas if $b > B/2$, then those central parts will be used for both sub-images[13]. The accuracy of the TEC reconstruction by means of image registration (sections 4 and 5.2) is affected by the choice of b in two ways. First, as the residual image displacement given by (72) (where b should be substituted instead of B) is proportional to the sub-image resolution $\frac{\pi c}{b}$, the increase of b reduces the distortions. Second, as the sub-bands are limited by the bandwidth of the original chirp, the frequency separation factor given by (71) with (D.2) decreases as b increases:

$$Z(b) = \frac{|\omega_1 - \omega_2|}{\omega_0} = \frac{B - b}{\omega_0}. \tag{D.3}$$

This, in turn, increases the distortions. The value of b minimizing the residual shift given by (72) in the split bandwidth setting is therefore

$$b^* = \arg\min_b \tilde{S}_R(b) = \arg\min_b \frac{\pi c}{b} \frac{\zeta_R}{2Z(b)} = \arg\min_b \frac{1}{b(B - b)} = \frac{B}{2}.$$

In other words, it corresponds exactly to the partition of the original chirp into two half-bandwidth chirps P_1 and P_2 given by (D.1)[14]. The actual minimum value is given by formula (72) with the substituted bandwidth $b^* = B/2$ and the frequency separation factor $Z(b^*) = B/(2\omega_0)$, see (D.3):

$$\tilde{S}_R = \frac{2\pi c \zeta_R \omega_0}{B^2}. \tag{D.4}$$

Similarly to (72), expression (D.4) does not depend on the ionospheric parameters.

By matching the residual range shift of (D.4) and the original range shift of (40), we obtain the sensitivity threshold of the split band implementation to the ionospheric TEC:

$$N_H = \frac{H}{R} \frac{m_e c}{e^2} \zeta_R \frac{\omega_0^3}{B^2}. \tag{D.5}$$

Formula (D.5) yields about 8 TECU for the parameters in table 1 and, according to (D.4), corresponds to $\tilde{S}_R \approx 70$ m. When the background value of the TEC is lower than that given by formula (D.5), it is not practical to use the split band version of dual carrier correction described in this appendix. This limitation, however, does not apply to the full-fledged version of the algorithm that employs two independent carrier frequencies with their respective bandwidths.

References

[1] Cheney M 2001 A mathematical tutorial on synthetic aperture radar *SIAM Rev.* **43** 301–12

[2] Ginzburg V L 1964 *The Propagation of Electromagnetic Waves in Plasmas* (*International Series of Monographs on Electromagnetic Waves* vol 7) (Oxford: Pergamon)

[3] Tsynkov S V 2009 On SAR imaging through the Earth's ionosphere *SIAM J. Imaging Sci.* **2** 140–82

[4] Parker S P (ed) *McGraw-Hill Dictionary of Scientific and Technical Terms* 6th edn (New York: McGraw-Hill)

[5] Meyer F J 2011 Performance requirements for ionospheric correction of low-frequency SAR data *IEEE Trans. Geosci. Remote Sens.* **49** 3694–702

[6] Smith E M and Tsynkov S V 2011 Dual carrier probing for spaceborne SAR imaging *SIAM J. Imaging Sci.* **4** 501–42

[7] Davies K and Smith E K 2002 Ionospheric effects on satellite land mobile systems *IEEE Antennas Propag. Mag.* **44** 24–31

[13] It is also possible to use sub-bands with different bandwidths, as suggested in [59].

[14] A similar yet not equivalent optimization formulation is analyzed in [40].

[8] van de Kamp M, Cannon P S and Terkildsen M 2009 Effect of the ionosphere on defocusing of space-based radars *Radio Sci*. **44** RS1003
[9] Wright P A, Quegan S, Wheadon N S and Hall C D 2003 Faraday rotation effects on L-band spaceborne SAR data *IEEE Trans. Geosci. Remote Sens*. **41** 2735–44
[10] Curlander J C and McDonough R N 1991 *Synthetic Aperture Radar. Systems and Signal Processing (Wiley Series in Remote Sensing)* (New York: Wiley)
[11] Meyer F, Bamler R, Jakowski N and Fritz T 2006 The potential of low-frequency SAR systems for mapping ionospheric TEC distributions *IEEE Geosci. Remote Sens. Lett*. **3** 560–4
[12] Rosen P A, Hensley S and Chen C 2010 Measurement and mitigation of the ionosphere in L-band interferometric SAR data *Proc. IEEE Int. Radar Conf. (Arlington, VA)* pp 1459–63
[13] Brcic R, Parizzi A, Eineder M, Bamler R and Meyer F 2010 Estimation and compensation of ionospheric delay for SAR interferometry *IGARSS 2010: Proc. IEEE Int. Geoscience and Remote Sensing Symp. (Honolulu, HI)* pp 2908–11
[14] Brcic R, Parizzi A, Eineder M, Bamler R and Meyer F 2011 Ionospheric effects in SAR interferometry: an analysis and comparison of methods for their estimation *IGARSS 2011: Proc. IEEE Int. Geoscience and Remote Sensing Symp. (Vancouver, Canada)* pp 1497–500
[15] Jehle M, Rüegg M, Zuberbühler L, Small D and Meier E 2009 Measurement of ionospheric Faraday rotation in simulated and real spaceborne SAR data *IEEE Trans. Geosci. Remote Sens*. **47** 1512–23
[16] Xiaoqing P, Freeman A, Chapman B, Rosen P and Zhenhong L 2011 Imaging ionospheric inhomogeneities using spaceborne synthetic aperture radar *J. Geophys. Res*. **116** 1–13
[17] Lee J-S and Pottier E 2009 *Polarimetric Radar Imaging from Basics to Applications* (Boca Raton, FL: CRC Press)
[18] Gail W B 1998 Effect of Faraday rotation on polarimetric SAR *IEEE Trans. Aerosp. Electron. Syst*. **34** 301–8
[19] Franceschetti G and Lanari R 1999 *Synthetic Aperture Radar Processing (Electronic Engineering Systems Series)* (Boca Raton, FL: CRC Press)
[20] Eichel P H and Jakowatz C V Jr 1989 Phase-gradient algorithm as an optimal estimator of the phase derivative *Opt. Lett*. **14** 1101–3
[21] Wahl D E, Eichel P H, Ghiglia D C and Jakowatz C V Jr 1994 Phase gradient autofocus—a robust tool for high resolution SAR phase correction *IEEE Trans. Aerosp. Electron. Syst*. **30** 827–35
[22] Li L and Li F 2008 Ionosphere tomography based on spaceborne SAR *Adv. Space Res*. **42** 1187–93
[23] Mattar K E and Gray A L 2002 Reducing ionospheric electron density errors in satellite radar interferometry applications *Can. J. Remote Sens*. **28** 593–600
[24] Jehle M, Frey O, Small D and Meier E 2010 Measurement of ionospheric TEC in spaceborne SAR data *IEEE Trans. Geosci. Remote Sens*. **48** 2460–8
[25] Zitová B and Flusser J 2003 Image registration methods: a survey *Image Vis. Comput*. **21** 977–1000
[26] Foroosh H, Zerubia J B and Berthod M 2002 Extension of phase correlation to subpixel registration *IEEE Trans. Image Process*. **11** 188–200
[27] Stone H S, Orchard M, Chang E-C and Martucci S 2001 A fast direct Fourier-based algorithm for subpixel registration of images *IEEE Trans. Geosci. Remote Sens*. **39** 2235–43
[28] Guizar-Sicairos M, Thurman S T and Fienup J R 2008 Efficient subpixel image registration algorithms *Opt. Lett*. **33** 156–8
[29] Tian Q and Huhns M N 1986 Algorithms for subpixel registration *Comput. Vis. Graph. Image Process*. **35** 220–33
[30] Abdou I E 1999 Practical approach to the registration of multiple frames of video images *Proc. SPIE* **3653** 371–82
[31] Kuglin C D and Hines D C 1975 The phase correlation image alignment method *Proc. IEEE Int. Conf. on Cybernetics and Society* pp 163–5
[32] Kuglin C D, Blumenthal A F and Pearson J J 1979 Map-matching techniques for terminal guidance using Fourier phase information *Proc. SPIE* **186** 21–29
[33] Tsynkov S V 2009 On the effect of start–stop approximation for spaceborne SAR imaging *SIAM J. Imaging Sci*. **2** 646–69
[34] Cheney M and Borden B 2009 *Fundamentals of Radar Imaging* (*CBMS-NSF Regional Conference Series in Applied Mathematics* vol 79) (Philadelphia, PA: SIAM)
[35] Smith E M 2013 SAR Imaging through the Earth's ionosphere *PhD Thesis* North Carolina State University, Raleigh, NC, USA in preparation
[36] Jakowatz C V, Wahl D E, Eichel P H, Ghiglia D C and Thompson P A 1996 *Spotlight-Mode Synthetic Aperture Radar: A Signal Processing Approach* (Berlin: Springer)
[37] Cumming I G and Wong F H 2005 *Digital Processing of Synthetic Aperture Radar Data* (Boston, MA: Artech House)

[38] Belcher D P 2008 Theoretical limits on SAR imposed by the ionosphere *IET Radar Sonar Navig.* **2** 435–48
[39] Manduchi R and Mian G A 1993 Accuracy analysis for correlation-based image registration algorithms *Proc. IEEE Int. Symp. on Circuits and Systems (Chicago, IL, 3–6 May 1993)* vol 1 (Piscataway, NJ: IEEE) pp 834–7
[40] Bamler R and Eineder M 2005 Accuracy of differential shift estimation by correlation and split-bandwidth interferometry for wideband and delta-k SAR systems *IEEE Geosci. Remote Sens. Lett.* **2** 151–5
[41] Armand N A 2005 Limitations to the resolution of satellite based synthetic aperture radars due to the conditions of the propagation of radio waves in the ionosphere *Explor. Earth Space* 27–38 (in Russian)
[42] Monin A S and Yaglom A M 1975 *Statistical Fluid Mechanics: Mechanics of Turbulence* vol 2 (Cambridge, MA: MIT Press)
[43] Lavrentiev M A and Shabat B V 1987 *Methods of the Theory of Functions in a Complex Variable* 5th edn (Moscow: Nauka) (in Russian)
[44] Monin A S and Yaglom A M 1971 *Statistical Fluid Mechanics: Mechanics of Turbulence* vol 1 (Cambridge, MA: MIT Press)
[45] Rytov S M, Kravtsov Y A and Tatarskii V I 1989 *Principles of Statistical Radiophysics: Wave Propagation Through Random Media* vol 4 (Berlin: Springer) (Translated from the second Russian edition by A P Repyev)
[46] Chorin A J and Hald O H 2006 *Stochastic Tools in Mathematics and Science* (*Surveys and Tutorials in the Applied Mathematical Sciences* vol 1*)* (New York: Springer)
[47] Gnedenko B V 1997 *Theory of Probability* 6th edn (Amsterdam: Gordon and Breach) (Engl. transl.)
[48] Chen J and Zebker H A 2012 Ionospheric artifacts in simultaneous L-band InSAR and GPS observations *IEEE Trans. Geosci. Remote Sens.* **50** 1227–39
[49] Liu J, Kuga Y, Ishimaru A, Xiaoqing P and Freeman A 2003 Ionospheric effects on SAR imaging: a numerical study *IEEE Trans. Geosci. Remote Sens.* **41** 939–47
[50] Gray A L, Mattar K E and Sofko G 2000 Influence of ionospheric electron density fluctuations on satellite radar interferometry *Geophys. Res. Lett.* **27** 1451–4
[51] Gilman M, Smith E and Tsynkov S 2012 A linearized inverse scattering problem for the polarized waves and anisotropic targets *Inverse Problems* **28** 085009
[52] Medina R, Penn J and Albanese R 2002 Dielectric response data on materials of military consequence *United States Air Force Research Laboratory Technical Report* AFRL-HE-BR-TR-2002-0155
[53] Gonzalez R C and Woods R E 2008 *Digital Image Processing* 3rd edn (New York: Prentice-Hall)
[54] Born M and Wolf E 1999 *Principles of Optics: Electromagnetic Theory of Propagation, Interference and Diffraction of Light* with contributions by ed A B Bhatia, P C Clemmow, D Gabor, A R Stokes, A M Taylor, P A Wayman and W L Wilcock 7th edn (expanded) (Cambridge: Cambridge University Press)
[55] Oughstun K E 2006 *Electromagnetic and Optical Pulse Propagation 1. Spectral Representations in Temporally Dispersive Media* (*Springer Series in Optical Sciences* vol 125) (New York: Springer)
[56] Ishimaru A, Kuga Y, Liu J, Kim Y and Freeman T 1999 Ionospheric effects on synthetic aperture radar at 100 MHz to 2 GHz *Radio Sci.* **34** 257–68
[57] Messier M A 1971 A standard ionosphere for the study of electromagnetic pulse propagation *EMP Technical Note* 117 (Air Force Weapons Laboratory)
[58] Ryaben'kii V S and Tsynkov S V 2007 *A Theoretical Introduction to Numerical Analysis* (Boca Raton, FL: Chapman and Hall)
[59] Rosen P A *et al* 2011 The proposed DESDynI mission—from science to implementation *RADAR: IEEE Radar Conf.* pp 1129–31